

Université du Québec
Institut National de la Recherche Scientifique
Centre Énergie, Matériaux et Télécommunications

CONTROLLING THE SYNTHESIS OF SILVER NANOSTRUCTURES FOR PLASMONIC APPLICATIONS

Par
Hongyan Liang

Thèse présentée pour l'obtention du grade de
Philosophiae doctor (Ph.D.)
en sciences de l'énergie et des matériaux

Jury d'évaluation

Président du jury et examineur interne	Andreas Peter Ruediger INRS-EMT
Examineur externe	Sylvain G. Cloutier École de Technologie supérieure
Examineur externe	Jung Kwon Oh Université Concordia
Directeur de recherche	Dongling Ma INRS-EMT
Codirecteur de recherche	Federico Rosei INRS-EMT

ABSTRACT

Silver nanostructures have been paid significant attentions in many applications due to their unique physical and chemical properties, which the bulk material does not possess. Controlling Ag nanostructures' size and shape to define their unique plasmonic features is important for practical applications. Generally, Ag nanostructures could be obtained through two main approaches, chemical and physical methods. Chemical method is the most widely used synthesis technique. That involves creation of Ag atoms from precursors by reduction and subsequent their growth into nanostructures with an aid of a stabilizer. Ag nanostructures with various well-controlled morphologies and sizes have been obtained from the solution phase. The size- and shape-dependent plasmonic features of Ag nanostructures have led to their wide applications in many fields, such as surface enhanced spectroscopy for sensors, catalysis and biological labeling. Driven by potential applications, the work performed in this thesis centers on the synthesis and properties of Ag nanostructures.

In the first part, synthesis and characterization of one dimensional (1D) Ag nanostructures were performed. To do so, two kinds of 1D silver nanostructures, silver 'nanorice' structures and 'nanocarrot' structures were synthesized through a facile polyol method. Polyethylene glycol 600 was used as a solvent and as a reducing agent, and polyvinylpyrrolidone (PVP) worked as capping agent. The main factor leading to the different morphologies of products is that the precursor of silver nitrate AgNO_3 was used for synthesis of silver nanorice structures while silver trifluoroacetate CF_3COOAg for nanocarrot structures. Their structure details were characterized by transmission electron microscopy and X-ray diffraction. The optical properties were characterized by ultraviolet-Vis-near infrared (UV-Vis-NIR) optical extinction spectra and electron energy loss spectroscopy (EELS). Their potential for sensor applications was tested by studying the effect of the change of environmental refractive index on the surface plasmon resonance (SPR) peak location.

In detail, Part I is divided into two sections based on two kinds of nanostructures (Section I and Section II). In Section I, the investigation was focused on studying the growth mechanism of silver nanorice structures and optimizing experimental conditions. By modifying synthesis parameters, Ag nanorice structures could be obtained on a large scale in high yield. Their growth

process was monitored for understanding their growth mechanism. The results showed the seed selection process, based on the oxidative etching of the twinned crystals, was an indispensable step for the growth of the nanorice structures and oxygen played a critical role in this seed selection process. The major shape development stage of the nanorice structures was dominated by the oriented attachment along the $\langle 111 \rangle$ direction, which was directed by the non-uniform capping of PVP on different facets. The Ostwald ripening was responsible for the seed growth into the primary nanoparticles (NPs) and the lateral growth of the nanorice structures albeit it was not straightforwardly apparent in the early stage of the anisotropic growth of the nanorice structures. Slightly increasing temperature showed the acceleration effect on the 1D growth along the $\langle 111 \rangle$ direction, while further increase in temperature led to the disappearance of the 1D shape and induced the formation of highly faceted, two-dimensional, truncated triangular and hexagonal plates mainly bound by low energy faces of $\{111\}$. The growth mechanism of these two-dimensional plates was remarkably different from that of the nanorice structures, and their growth was controlled by diffusion and dictated by the twin plane. The longitudinal SPR of the nanorice structures synthesized herein was highly sensitive to the surrounding dielectric medium, with the refractive index sensitivity as high as 820 nm/RIU (RIU, per refractive index unit), which makes them highly promising for sensor applications. Furthermore, in addition to the longitudinal resonance, the multipolar resonances in individual nanorice structures were mapped in real space by using the high-resolution EELS technique.

In Section II, we focused on the synthesis of asymmetric Ag nanocarrot structures and corresponding characterization of their crystal structures and optical properties. Asymmetric 1D silver nanocarrot structures were synthesized in high yield for the first time. Structure characterization showed that the face centered cubic dominated, crystalline silver nanocarrot structures feature mixed twins and stacking faults along the $\langle 111 \rangle$ longitudinal direction. The crystal structure of Ag nanocarrot structures was the same as that of silver nanorice structures. The SPR characteristics of the nanocarrot structures were revealed by UV-Vis-NIR optical extinction spectroscopy on particle ensembles and by nanoscale EELS on individual nanocarrot structures. The results from both techniques were further supported by calculations. Multipolar plasmon resonances, observed by EELS, showed an interesting asymmetric distribution over the length of the ‘nanocarrot’, in contrast to the symmetric distribution observed in the ‘nanorice’ structures. The longitudinal SPR peaks were red shifted and amplified in optical spectra with

increasing nanocarrot length. Silver nanocarrot structures also showed high refractive index sensitivity of 890 ± 87 nm/RIU, which making them very attractive for sensor applications. In addition, these nanocarrot structures are also promising for, but not limited to, biological sample studies due to their tunable SPR in the NIR spectral range and optical waveguiding below the diffraction limit.

Part II is focused on the surface enhanced spectroscopy investigations based on silver nanostructures and is divided into two sections, corresponding to surface enhanced Raman scattering (SERS) (Section III) and surface enhanced fluorescence (Section V), respectively. In Section III, we focused on investigating the SERS of flower-like silver mesoparticle dimers. The dimers were performed in a controlled manner by means of micro-manipulation. The measured SERS enhancements were found to be 10~100 times higher on dimers than that on individual mesoparticles. The observation of high dependence of SERS on incident polarization illustrates that, even though the surface roughness is dominant for SERS on the individual mesoparticles with rough surface topography, the coupling effect still gives significant additional SERS enhancement in their dimers. In addition, the use of the micro-manipulator allows us to achieve dimers with high SERS enhancement controllably and reproducibly. This work contributed to the understanding the SERS enhancement mechanism in the roughened mesoparticle dimer system, as well as to controllably realizing SERS substrates with large “hot spot” area for high enhancement.

In Section V, we focused on the photoluminescence (PL) enhancement in the plasmon/fluorophore system consisting of lead chalcogenide quantum dots (QDs) and Ag NPs film to investigate the interaction between QDs and plasmonic structures. Ag NPs instead of Ag “nanorice” or “nanocarrot” structures were used here because the high stability of NPs makes it easier to claim to concept for completing the preliminary work. The Ag NP/QD films were fabricated by a layer-by-layer approach. The films exhibited significant PL enhancement, dominated by the excitation enhancement mechanism when the spectra of the Ag NPs did not match the emission band of QDs and the excitation wavelength was far away from the SPR peak in the NIR range. In contrast, both the excitation and emission enhancement mechanisms could contribute to the PL enhancement when the absorption/emission spectra of QDs matched the resonance wavelengths of Ag NPs. Moreover, by optimizing the Ag NP/QD system, we were

able to reach a PL enhancement factor as high as 2.8, due to the strong coupling between the QDs and Ag NPs. Therefore, these Ag NP/QD films hold great promise for emerging QD devices for potential applications, such as highly efficient light-emitting diodes and biological sensors.

ACKNOWLEDGEMENTS

Foremost, I would like to express my sincere gratitude to my supervisors Prof. Dongling Ma and Prof. Federico Rosei for the continuous support of my Ph.D study and research, for their patience, motivation, enthusiasm, and immense knowledge. Their precious advice and direction helped me in all the time of research and writing of this thesis. They have created a warm and stimulating research environment allowing me explore a complex and fascinating scientific field. I could not have imagined having better supervisors and mentors for my Ph.D study.

I thank to Prof. Hongxing Xu, Prof. Gianluigi A. Botton, Prof. Wenzhong Wang, Prof. Nianqiang Wu, and Prof. Zhipeng Li for their important comments during my project research.

I want to acknowledge the contributions to this work made by Dr. Haiguang Zhao, who gave me invaluable help and collaboration. I gratefully acknowledge my collaborators, Dr. David Rossouw, Dr. Scott K. Cushing, Dr. Guozhu, Dr. Honglong Shi and Dr. Catalin Harnagea. I am grateful to Wei Huang's help for the French translation. Thanks to all the group members for their help throughout the work. I am grateful to have been part of such supportive, hardworking, and inspiring groups. These people include: Jianming Zhang, Stephano Desian, Defa Wang, Ibrahima Ka, Belete Atomsa Gonfa, Fuqiang Ren, Long Tan, Maxime Gougis, Zhenghe Xu and Mee Rahn Kim. I have to pay special thanks to Prof. Shuhui Sun, Dr. Gaixia Zhang, Youling Wang, Shun Li, Yue Huang, Yi Hu, Bo Li and Lijun Wang, they always cheer me up.

I thank to the departmental and technical staff at INRS-EMT.

I would like to thank Jean-Philippe Masse at Ecole Polytechnique for measurements.

I am eternally grateful to my parents, who have been a constant source of love. I would like to thank to my husband, Kaiyan Zhang, who loves me deeply and supports me selflessly. I want to tell them, I love you. I thank my family and my friends for their continuing love and heartily support.

Finally, I wish to acknowledge the following organizations for their financial support: the Natural Sciences and Engineering Research Council of Canada and Fonds de la recherche sur la nature et les technologies for Ph.D Program.

CONTENTS

CHAPTER 1	INTRODUCTION.....	1
1.1	Plasmonics.....	2
1.2	Plasmonics in Nanostructures	5
1.3	Plasmonic Applications.....	7
1.3.1	Surface Enhanced Raman Scattering.....	7
1.3.2	Surface Enhanced Fluorescence	10
1.3.3	Optical Detection of the Change in Refractive Index.....	13
1.4	Synthesis of Silver Nanostructures	14
1.4.1	Unique Properties of Silver Nanostructures	14
1.4.2	Synthesis of Silver Nanostructures.....	15
1.5	Thesis Objectives and Organization.....	18
1.5.1	Our Objectives	18
1.5.2	Organization of the Thesis.....	20
CHAPTER 2	EXPERIMENTAL, CHARACTERIZATION AND THEORETICAL MODELING	22
2.1	Materials.....	22
2.2	Synthesis of Silver Nanostructures	22
2.2.1	Silver Nanorice Structures	23
2.2.2	Silver Nanocarrot Structures.....	24
2.2.3	Flower-like Silver Mesoparticles.....	25
2.2.4	Silver Nanospheres	26
2.3	Synthesis of Quantum Dots.....	26
2.3.1	PbS Quantum Dots.....	27
2.3.2	PbS/CdS Quantum Dots.....	27

2.4	Preparation of Sample for Studying Refractive Index Effect	28
2.4.1	Preparation of A Monolayer of Silver Nanorice Structures.....	28
2.4.2	Preparation of Silver Nanocarrot Structure Solution	29
2.5	Preparation of Samples for Surface Enhance Spectroscopy	29
2.5.1	Preparation of Samples for Surface Enhance Raman Scattering	29
2.5.2	Preparation of Ag NP/QD Films for Surface Enhanced Fluorescence	30
2.6	Studying Morphology, Crystal Structure and Composition.....	30
2.6.1	Scanning Electron Microscopy	30
2.6.2	Transmission Electron Microscopy and Selected Area Electron Diffraction.....	30
2.6.3	Energy Dispersive X-ray Spectroscopy	31
2.6.4	Powder X-ray Diffraction	32
2.7	Studying Optical Properties	32
2.7.1	Electron Energy-Loss Spectroscopy	32
2.7.2	Extinction Spectroscopy	33
2.7.3	Raman Spectroscopy.....	34
2.7.4	Steady-state and Time-resolved Photoluminescence Spectroscopy	35
2.8	Theory	35
2.8.1	Mie Theory.....	36
2.8.2	Finite-Difference Time-Domain Simulation.....	36
2.8.3	Boundary Element Method.....	36
CHAPTER 3	RESULTS.....	38
3.1	Part I: Synthesis.....	38
	Section I Silver Nanorice Structures: Oriented Attachment-Dominated Growth, High Environmental Sensitivity and Real-Space Visualization of Multipolar Resonances.....	39
	Section II Asymmetric Silver “Nanocarrot” Structures: Solution Synthesis and Their Asymmetric Plasmonic Resonances	53

3.2	Part II: Investigation of Potential Applications.....	65
	Section III Enormous Surface Enhanced Raman Scattering from Dimers of Flower-like Silver Mesoparticle.....	66
	Section IV Photoluminescence Enhancement of Near-infrared Emitting PbS and PbS/CdS Core/shell Quantum Dots Induced by Silver Nanoparticle Film.....	77
CHAPTER 4	CONCLUSIONS AND PERSPECTIVES	87
4.1	Conclusions	87
4.2	Perspectives	89
REFERENCES	92
RÉSUMÉ	96

LIST OF TABLES

Table 1.1 Summary of the Shapes, LSPR absorption peaks, demonstrated applications, and methods for synthesis of Ag nanostructures ^aThe main absorption peak (nm). ^b Assembly means the nanostructure has been assembled into larger structures for plasmonic applications or studies. The red lines in the illustration refer to a crystalline plane; the dark faces are {100}, and the light faces are {111}. The table was taken from reference [6].

LIST OF FIGURES

Figure 1.1 Davos seaworth stained glass window. The graph was taken from internet.
<http://guad.deviantart.com/art/Davos-Seaworth-Stained-Glass-Window-330453541>

Figure 1.2 The Lycurgus Cup in reflected (left, green color) and transmitted (right, red color) light. Height: 16.5 cm (with modern metal mounts), diameter: 13.2 cm. © The Trustees of the British Museum. The graph was taken from internet.
<http://www.forumancientcoins.com/numiswiki/view.asp?key=cage%20cup>

Figure 1.3 Schematic illustration of the two types of plasmonic nanostructures excited by the electric field (E_0) of incident light with wavevector (k). In (A) the size of nanostructure is smaller than the wavelength of light and the free electrons can be displaced from the lattice of positive ions (consisting of nuclei and core electrons) and collectively oscillate in resonance with the light. This is known as a LSPR. In (B) the nanowire has one dimension much larger than the wavelength of light. In this case, light coupled to the nanostructure will excite the free electrons to create a PSP that can travel along the surface of the metal nanostructure. The schematic illustration was taken from reference [6].

Figure 1.4 (A–D) TEM images of Ag nanocubes with edge lengths of 36, 58, 99, and 172 nm, respectively. In (E) the LSPR of the nanocubes red shifts as the edge length of the nanocubes increases. The graph was taken from reference [6].

Figure 1.5 The different possibilities of visual light scattering: Rayleigh scattering (no exchange of energy so the incident and emitted photons have the same energy), Stokes scattering (the atom or molecule absorbs energy and the emitted photon has less energy than the absorbed photon) and anti-Stokes scattering (the atom or molecule loses energy and the emitted photon has more energy than the absorbed photon). The graph was taken from internet.
<http://en.wikipedia.org/wiki/File:Ramanscattering.svg>

Figure 1.6 Schematic of SERS. The SERS spectrum shown as an example was collected from 10^{-9} M adenine in a solution of silver nanoaggregates. The SERS signal P_{SERS} depends on excitation intensity I_L and an effective SERS cross section $\sigma_{eff}^{SERS} = \sigma_{ads}^R A(\nu_L)^2 A(\nu_S)^2$, which benefits from the EM enhancement described by field EFs $A(\nu_L)$ and $A(\nu_S)$ for the excitation and scattered field, and a chemical SERS effect, described by an increased Raman cross section σ_{ads}^R of the adsorbed molecule compared to the cross section in a “normal” Raman experiment σ^R . N is the number of molecules involved in the SERS process. The graph was taken from reference [45].

Figure 1.7 Jablonski diagram. After an electron absorbs a high energy photon the system is excited electronically and vibrational. The system relaxes vibrational, and eventually fluoresces at a longer wavelength. The graph was taken from internet. <http://www.olympusmicro.com/primer/techniques/fluorescence/fluorescenceintro.html>

Figure 1.8 Mechanisms of various light scattering processes. (a) Rayleigh, (b) nonresonance Raman, (c) pre-resonance Raman, (d) resonance Raman resonance fluorescence (e) relaxed fluorescence. The graph was taken from the website of Horiba Scientific. <http://www.azom.com/article.aspx?ArticleID=2950>

Figure 1.9 Polyol method for synthesizing Ag nanostructures. In (A) the reduction of Ag ions by EG leads to the formation of nuclei that are highly volatile. As the nuclei grow, fluctuations cease and their structure becomes static and contains multiply twinned boundary defects, singly twinned boundary defects, or are single crystalline with no boundary defects. These seeds are then grown into different nanostructures like (B) spheres, (C) cubes, (D) truncated cubes, (E) right bipryamids, (F) bars, (G) spheroids, (H) triangular plates, and (I) wires. The red lines in the illustration refer to a twin plane; the dark faces are {100}, and the light faces are {111}. The graph was taken from reference [6].

Figure 2.1 Schematic illustration of the setup for Ag nanostructures preparation.

Figure 2.2 Schematic illustration of the air-free reaction setup for synthesizing QDs.

Figure 2.3 Schematic illustration of the synthesis of thin-shell PbS/CdS QDs by cation exchange.

Figure 2.4 Schematic illustration of EDX. The graph was taken from internet. <http://commons.wikimedia.org/wiki/File:EDX-scheme.svg>

Figure 2.5 The nanoscale spectroscopy of a silver nanowire (blue) and nanoslot (red) probed by EELS (insert on the right). The graph was taken from reference [3].

Figure 2.6 a, Schematic illustration of the confocal Raman system. The optical path 1 is for the Raman imaging, and the optical path 2 is for the measurement of Raman spectra. b, Sketches for Raman image and spectra acquisition. When using the image function, mirrors 1&4 are moved into the optical path, and the optical path 2 is thus blocked. The laser is focused on one end of the Ag wire through an objective, the Raman signals from the sample are collected by the same objective. After passing the Rayleigh filter, the optical signals go through an angle dependent narrow band pass filter, which permits one Raman peak ($\pm 20 \text{ cm}^{-1}$) pass, and arrive at the TE air cooled 576×400 CCD to produce an image. To acquire remote Raman spectra, mirrors 1&4 should be moved out of the path, and the confocal Raman spectral acquisition mode marked with path 2 is then used for collecting Raman spectra with the same CCD. The top left, bottom left and bottom right mirrors need to be adjusted to move the laser focus point to the

position for plasmon excitation, e.g. one end of the Ag nanowire. The graph was taken from reference [28].

LIST OF CHEMICAL COMPOUNDS, ABBREVIATIONS AND SYMBOLS

Chemical compounds

AgNO ₃	silver nitrate
CdO	cadmium oxide
CF ₃ COOAg	silver trifluoroacetate
C ₆ H ₈ O ₆	ascorbic acid
HCl	hydrochloride acid
HNO ₃	nitric acid
NaSH	sodium hydrosulfide
PbCl ₂	lead (II) chloride
S	sulfur

Abbreviations

ADF	annular dark field
BEM	boundary element method
EDS	energy dispersive X-ray spectroscopy
EELS	electron energy-loss spectroscopy
EG	ethylene glycol
EM	electromagnetic
FCC	face centered cubic
FDTD	finite-difference time-domain
FOM	figure of merit
FP	Fabry-Pérot
HRTEM	high resolution transmission electron microscopy
LSP(s)	localized surface plasmon(s)

LSPR	localized surface plasmon resonance
MGITC	malachite green isothiocyanate
NIR	near-infrared
NP(s)	nanoparticle(s)
OA	oleic acid
ODE	octadecene
OLA	oleylamine
1D	one dimensional
PEG	polyethylene glycol
PL	photoluminescence
PMMA	polymethylmethacrylate
PSP(s)	propagating surface plasmon(s)
PVP	poly(vinyl pyrrolidone)
QD(s)	quantum dot(s)
RIU	refractive index unit
SAED	selected area electron diffraction
SEF	surface enhanced fluorescence
SEM	scanning electron microscopy
SERS	surface enhanced Raman scattering
SP(s)	surface plasmon(s)
SPP	surface plasmon polariton
SPR	surface plasmon resonance
TEM	transmission electron microscopy
THF	tetrahydrofuran
UV	ultraviolet
Vis	visible

XRD	X-ray diffraction
Symbols	
P_{abs}	absorption power
σ	effective cross sections
σ_{abs}	effective cross sections of absorption
σ_{sca}	effective cross sections of scattering
E_0	energy of a photon
$A(\nu_L)$	enhancement factors for the excitation field
$A(\nu_S)$	enhancement factors for the scattered field
ω	frequency
I	incident intensity
σ_{ads}^R	Raman cross section
P_{sca}	scattering power
S	surface plasmon resonance sensitivity
λ	the wavelength
k	wavevector
λ_p	wavelength of peak shift

CHAPTER 1 INTRODUCTION

In human history, three nonradioactive members of Group 11 in the periodic table, copper (Cu), silver (Ag), and gold (Au) have played an important role since they are used to mint coins.[1] Coinage metals have shining appearance due to their excellent reflective properties for visible (Vis) light and intense color by coupling to light.[2] Their fascinating optical performance has drawn plentiful applications. Coinage metal nanoparticles (NPs) have been exploited by artisans since the days of the Roman Empire as colorants in cloths, stained glasses (Figure 1.1) and ceramics.[3, 4] Lycurgus cup [5] represents the outstanding achievement of the application of metal's optical properties (Figure 1.2). The Lycurgus Cup is made by the Romans dating back to the fourth century. When viewed in reflected light (e.g., in daylight) it appears green, and when viewed in transmitted light (i.e., light is shone into the cup and transmitted through the glass), it appears red.[5] These typical cases are the applications of surface plasmon resonance (SPR) in ancient times. Today, the research of SPR has attracted much interest due to its ability of efficiently manipulating light on a deep sub-wavelength scale and its potential applications, which goes far beyond decorations.



Figure 1.1 Davos seaworth stained glass window. The graph was taken from internet. <http://guad.deviantart.com/art/Davos-Seaworth-Stained-Glass-Window-330453541>

The growing field of research on SPR has been focused on maneuvering the metal-light interactions, which is known as “plasmonics”.[2, 6, 7] In this branch of research, metal nanostructures serve as antennas to convert light into localized electric fields, as sensors to detect

the change of the local dielectric environment, and as wave guides to confine and route light below the classical diffraction limit. These properties can result in many applications, such as chemical and biochemical sensors,[8-10] surface enhanced spectroscopy for sensors,[11-13] photothermal therapy[12, 14, 15] and nanophotonic waveguides and so on.[16-18] All these applications strongly depend on the metal-light interactions. With precisely controlled size, shape, and/or spacing of nanostructures, light can be effectively manipulated and controlled with unprecedented accuracy.[14] The development of new methods make it is possible to realize this level of control.[19-22] Such exquisite synthetic control and advanced detection instruments in combination with powerful electromagnetic (EM) modeling tools have provided a better understanding of the metal-light interactions.[10] Of the metals, Ag has attracted interest in the research of plasmonics, and its advantageous properties have led to most applications in relevant fields.[6, 21, 23]



Figure 1.2 The Lycurgus Cup in reflected (left, green color) and transmitted (right, red color) light. Height: 16.5 cm (with modern metal mounts), diameter: 13.2 cm. © The Trustees of the British Museum. The graph was taken from internet. <http://www.forumancientcoins.com/numiswiki/view.asp?key=cage%20cup>

1.1 Plasmonics

In physics, a plasmon in metal is the quantized collective oscillation of conduction electrons excited by EM radiation.[18, 24, 25] In a classical picture, mobile free electrons repel each other and are attracted to the fixed positive ion cores in a metal. Under an external time-varying EM field, electrons will be forced to oscillate collectively against the restoring force of positive nuclei until the energy is lost as a result of resistance or damping. When the frequency of external EM field (light) is below the metal's plasmon frequency, the electrons will screen the

electric fields of light and the light is reflected. On the contrary, when the incident frequency is above the metal's plasmon frequency, the response of electrons could not be quick enough and the incident waves are transmitted instead.[2] The ability of a metal nanoparticle to support an SP is dependent on its dielectric function ϵ , which includes a real part (describing the strength of the polarization induced by an external electric field) and an imaginary part (describing the loss encountered in polarizing the material). Both factors vary with excitation wavelength (λ). Thus, a small value of imaginary part is important to minimize the loss. To achieve the resonance condition, a negative real part of dielectric constant is necessary, which is not possible for standard dielectrics and nonmetals that typically have positive values. At the same time, the imaginary dielectric constant should be close to zero to support a strong resonance. The performance of the plasmon in a metal, which has a negative real and small positive imaginary dielectric constant, can be quite pronounced because its plasma frequency generally falls in the visible (Vis) spectral range and it has a high electrical conductivity. Among the metallic elements, silver has the best performances at optical frequencies with lowest energy loss. Gold is often the choice at lower frequencies, having the advantage of being chemically stable in many environments. However, the interband losses of gold in the Vis spectrum (< 500 nm) are high. Similarly, copper is plagued by large interband losses over most of the Vis spectrum. Thus, silver and gold have predominately been the choice for plasmonic applications.[2, 26]

Bulk (or volume) plasmons are the quantized bulk oscillations of electrons.[2] The frequency is defined as[2]

$$\omega_p^2 = \frac{n e^2}{\epsilon_0 m} \quad (1)$$

where n is the electron density, e is the electron charge, ϵ_0 is the relative permittivity of free space and m is the electron mass. It must be noted that the bulk here refers to a material with all three dimensions much larger than the wavelength of light.[9] Surface plasmons (SPs) are those tightly bound to the metal-dielectric interface.[9] They have lower energy than bulk (or volume) plasmons and can couple with photons to result in a quasi-particle called a surface plasmon polariton (SPP).[10]

Two types of plasmonic modes exist: (i) nonpropagating localized surface plasmons (LSPs) and (ii) propagating surface plasmons (PSPs).[2, 6] LSPs are supported by nanostructures with a size

smaller than or comparable with the excitation wavelength in three dimensions, as shown in Figure 1.3A. In this case, the structures experience a nearly uniform EM field associated with the light (E_0).[6] Two effects are important for LSPs. First, LSPs, once excited, have the striking ability to squeeze light into nanometer dimensions, producing the large local enhancement of EM energy. The EM field reaches its maximum at the interface, and exponentially decays away from the surface. Second, the LSPs can be excited when the excitation frequency (ω) matches their natural frequency, and strong resonance occurs, commonly known as localized surface plasmon resonance (LSPR). LSPR results in strong light scattering, intense absorption and the maximum enhancement of the local EM field.[9] The frequency and intensity of LSPR depend on the composition, size, and shape of nanostructures and their dielectric environments.

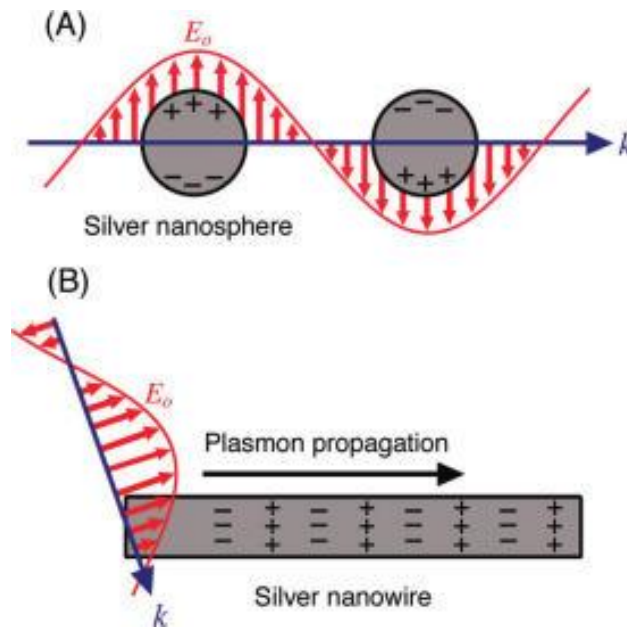


Figure 1.3 Schematic illustration of the two types of plasmonic nanostructures excited by the electric field (E_0) of incident light with wavevector (k). In (A) the size of nanostructure is smaller than the wavelength of light and the free electrons can be displaced from the lattice of positive ions (consisting of nuclei and core electrons) and collectively oscillate in resonance with the light. This is known as a LSPR. In (B) the nanowire has one dimension much larger than the wavelength of light. In this case, light coupled to the nanostructure will excite the free electrons to create a PSP that can travel along the surface of the metal nanostructure. The schematic illustration was taken from reference [6].

PSPs are supported by structures with one or two dimensions larger than the wavelength of incident light, as described in Figure 1.3B. They can travel along the metal surface up to hundreds of micrometers.[10] The associated EM field also decays exponentially from the

interface. In particular, in one dimensional (1D) nanostructures, SPs could be excited and propagate back and forth between two ends, behaving like Fabry-Pérot (FP) resonators.[6, 27] By controlling the morphology of the structure, the propagation distance (tens of micrometers in nanowires) and the PSP waves can be manipulated.[6, 28] The investigation of light-metal interactions is known as “plasmonics”, which is related to the localization, guiding, and manipulation of EM waves beyond the diffraction limit and down to the nanometer-length scale.[6, 18, 24, 26] The extraordinary advances in fabrication (such as electron-beam lithography, wet-chemical synthesis and focused ion-beam milling), characterization of metal nanostructures, (such as scanning electron microscopy (SEM), dark-field and near-field optical microscopies) and the emergence of EM simulation tools (based on Mie theory, discrete dipole approximation, boundary element method (BEM) and finite-difference time-domain (FDTD) methods) allowed the rapid development of the field of plasmonics.[24, 26]

1.2 Plasmonics in Nanostructures

The LSPR of metal nanostructures is attributed to the collective oscillation of electrons.[14, 29, 30] When light interacts with metal nanostructures, LSPR is excited and the incident light is dissipated in the form of heat within the nanostructures, which results in strong absorption or reradiated into free space which is scattering.[26] To understand in depth how the metal-light interact, which strongly depends on the particle geometry and dielectric environment, we must turn to theory. Basically, effective cross section (σ) has been used to describe the absorbed or scattered power. σ of absorption (σ_{abs}) and scattering(σ_{sca}) is defined as the ratio of the absorption (P_{abs}) and scattering (P_{sca}) power (photons s^{-1}) to the incident intensity (I , photons $s^{-1} cm^{-2}$), respectively, as described below:[26]

$$\sigma_{abs} = P_{abs}/I \quad (2)$$

$$\sigma_{sca} = P_{sca}/I \quad (3)$$

The extinction cross section is thus defined as:

$$\sigma_{ext} = \sigma_{abs} + \sigma_{sca} \quad (4)$$

When the LSPRs happen, the extinction cross section could be increased by several times.

The size and shape of nanostructures have a critical effect on the plasmonic features, such as frequency, bandwidth and intensity of LSPR.[31] The size of a nanoparticle determines plasmonic features that include the ratio of absorption to scattering, the number of LSPR modes, the peak position of an LSPR mode, and the extent of PSP localization.[6] For small spherical nanoparticles, they generally exhibit one dipole mode when their radius R is much smaller than the wavelength of light. The σ_{abs} and σ_{sca} are directly proportional to R^3 and R^6 , respectively. When R is smaller than ~ 30 nm, the LSPR extinction is dominated by absorption.[2, 27, 32] When the size of particles increases, they will scatter light more efficiently.[17] At the same time, the peak position of LSPR will red shift and the width will broaden due to the larger charge separation. Higher order modes will appear as well. In another case, as shown in Figure 1.4, with the increase of the silver nanocube size, the peak position of LSPR shifts to red accompanied by the broadening of the peak.

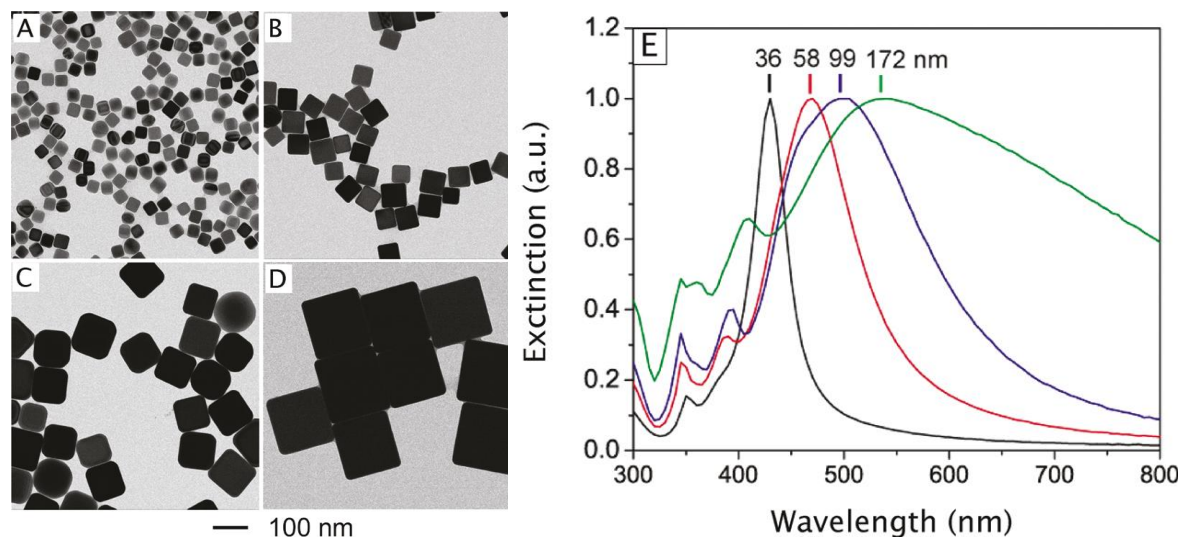


Figure 1.4 (A–D) Transmission electron microscopy (TEM) images of Ag nanocubes with edge lengths of 36, 58, 99, and 172 nm, respectively. In (E) the LSPR of the nanocubes red shifts as the edge length of the nanocubes increases. The graph was taken from reference [6].

Shape is another critical parameter for plasmonic features.[33] When the symmetry of a structure decreases, the number of resonances increases because the electrons could be polarized in more ways. At the same time, the dipole mode is lower due to lacking centrosymmetry. With the appearance of sharp corners, the LSPR peaks redshift due to a greater charge separation. Via different synthesis approaches, Ag nanostructures of different shapes, such as nanospheres,

nanocubes, nanorice structures and nanowires, have been achieved.[23] The spherical Ag NPs in general only show one SPR peak, but in a big contrast, 1D structures, such as nanobars and nanorice structures, support both transverse and longitudinal resonances, with the latter tunable from the Vis to near-infrared (NIR) spectral range by controlling the aspect ratio (length/diameter) and/or length.[15, 34] In addition, with increasing aspect ratio, higher order multipolar SPR modes, which behave like FP resonators, can be excited.[27, 35-37]

Tailoring the size and shape of metal NPs allows the tuning of the SPR to a desired frequency, and also offers the opportunity to achieve the highest possible enhancement of the EM field. For example, sharp surface curvatures and tips (in prisms[8]or rods [38]) as well as junctions (in core/shell structures[39] or dimers[8]) can yield a large EM enhancement. In the last two decades, the development of nanofabrication techniques allows the manipulation of NP geometries and assemblies.

1.3 Plasmonic Applications

Up to now, numerous applications based on plasmonics have emerged, which can be categorized into three thrusts: (i) taking advantage of the nanostructures' ability as antennas to concentrate light into localized electric fields to enhance or modify the optical features of nearby reporters, such as surface enhanced spectroscopy for sensor applications;[40, 41] (ii) exploiting the sensitivity of nanostructures' LSPR properties toward their local dielectric environments to detect the change on the metal surface or of surroundings for applications, such as LSPR-based chemical and biochemical sensing and detection;[10, 14, 42] (iii) acting as waveguides to confine and route light with plasmonic circuitry.[24, 43, 44] Herein, some typical applications in the thrusts mentioned above are discussed in the following section.

1.3.1 Surface Enhanced Raman Scattering

Raman scattering is inelastic scattering of light as a result of its interaction with matter.[45, 46] Raman spectroscopy is used as a powerful tool for chemical analysis, which gives spectral fingerprints, characteristic of Raman active molecules and it is sensitive to composition, bond strength, environment, and structure. Although the inelastic scattering of light was predicted by Adolf Smekal in 1923, it was not observed in experiment by Sir Chandrasekhara Venkata Raman

and Kariamanickam Srinivasa Krishnan until 1928, and was then named as Raman effect.[13] For the spontaneous Raman effect, a photon excites the molecule from the ground state to a virtual energy state. When the molecule relaxes, it emits a photon and returns to a different rotational or vibrational state. The difference in energy between the original state and this new state leads to a shift in the emitted photon's frequency away from the excitation wavelength (Figure 1.5). The Raman scattering intensity P_{RS} is determined by excitation intensity I_L and the Raman cross section σ_{RS} . σ_{RS} depends on the polarizability derivative of the molecular vibration.[45] In most cases, the number of inelastically scattered photons is extremely small, due to rather low Raman scattering cross sections (σ_{RS}) of 10^{-30} – 10^{-25} cm² per molecule, although higher values may be obtained under resonance conditions.[10, 45] The small Raman cross sections require a larger number of molecules to be involved for detection. As a consequence, the use of Raman spectroscopy in ultrasensitive trace detection is limited.

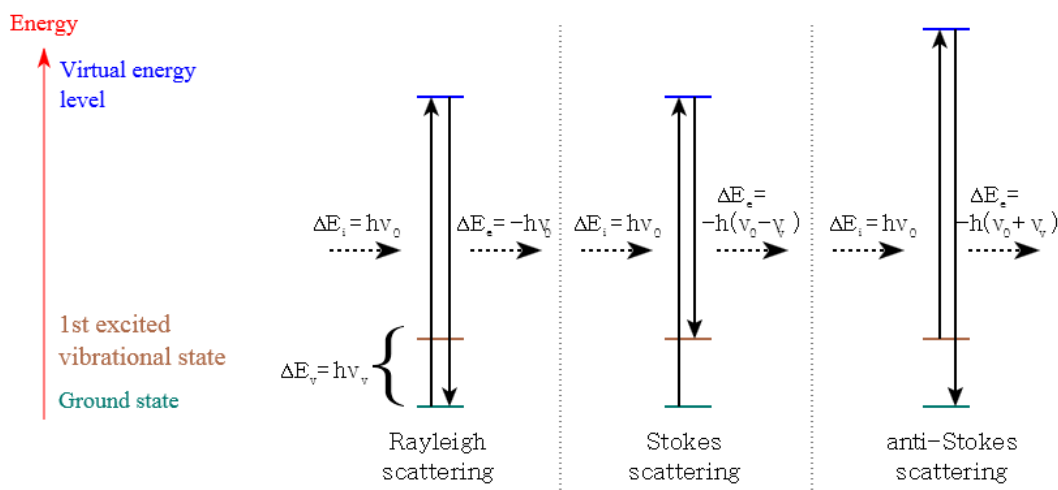


Figure 1.5 The different possibilities of visual light scattering: Rayleigh scattering (no exchange of energy so the incident and emitted photons have the same energy), Stokes scattering (the atom or molecule absorbs energy and the emitted photon has less energy than the absorbed photon) and anti-Stokes scattering (the atom or molecule loses energy and the emitted photon has more energy than the absorbed photon). The graph was taken from internet. <http://en.wikipedia.org/wiki/File:Ramanscattering.svg>

In 1970s, Jeanmaire, Van Duyne, Albrecht and Creighton independently observed that adsorption of pyridine onto electrochemically roughened Ag surfaces could increase the Raman scattering intensity by a factor of $\sim 10^6$. [7, 13, 47, 48] This striking discovery was denoted the surface enhanced Raman scattering (SERS) effect (Figure 1.6). SERS effect can handle the

problem mentioned before; however, its widespread application was limited by obstacles such as the irreproducibility of substrates. The development of nano-fabrication techniques have significantly contributed to obtaining reliable, reproducible and highly-sensitive SERS substrates. As a result, there has been a renewed interest in Raman spectroscopy as exciting advances of the past 10–15 years.[7, 19, 40, 49] Using metal nanostructures, SERS intensities could reach the single-molecule detection level with enhancement factors (EFs) up to 10^{15} . [11, 47]

Several theories have been developed to explain the origin of SERS, with “EM field enhancement”[24, 50] and “chemical enhancement”[51] being generally accepted ones. In EM field theory, an amplified EM field can give rise to EFs of 10^{10} – 10^{11} . [24, 50] This effect is provided by SPs transferring energy to the analytes through focusing light to generate the enhanced EM field. When the incident light strikes the surface, localized SPs are excited. The field enhancement is greatest at resonance. In order for scattering to occur, the plasmon oscillations must be perpendicular to the surface because scattering will not take place with in-plane oscillations. Because of this requirement, roughened surfaces or arrangements of nanostructures are typically required. The SERS effect can be quite pronounced because the field enhancement occurs twice. Firstly, the field enhances the incident light and secondly, the field enhances the Raman scattering, resulting in further increase in the total output. At each stage the electric field is enhanced as $|E|^2$, for a total enhancement of $|E|^4$. [45] The enhancement is not equal for all frequencies. When the frequency shift between Raman signal and the incident light is small as compared to the width of the SPR, both the incident light and the Raman signal can be at resonance with the plasmons, leading to the $|E|^4$ enhancement with $A(\nu_L) \cong A(\nu_S)$. When the frequency shift is large, the incident light and the Raman scattering cannot both be on resonance, thus the enhancement cannot be maximal. For this reason, Au, Ag and Cu are considered as best metals for SERS because their SPR falls in the Vis and NIR range. [45] The second and less prominent mechanism is the “chemical enhancement” or “electronic enhancement”, [51] which arises from metal-molecule interactions. Metal-molecule charge transfer can take place, which modifies the electronic states of molecules and alter their Raman cross section, leading to more efficient Raman scattering. [45] This type of enhancement is sensitive to the surface properties of SERS substrates and the nature of analyte molecules. It is thought to be responsible for at most two orders of magnitude of the enhancement. The large of contribution from the EM field enhancement has made it a preferred route for SERS investigations. Therefore, choice of SERS

substrates and excitation wavelength are critical factors for observing maximal Raman enhancement.

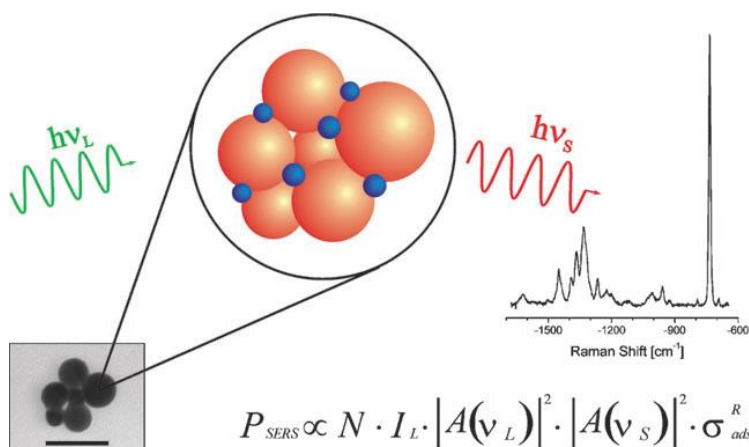


Figure 1.6 Schematic of SERS. The SERS spectrum shown as an example was collected from 10^{-9} M adenine in a solution of silver nanoaggregates. The SERS signal P_{SERS} depends on excitation intensity I_L and an effective SERS cross section $\sigma_{eff}^{SERS} = \sigma_{ads}^R A(\nu_L)^2 A(\nu_S)^2$, which benefits from the EM enhancement described by field EFs $A(\nu_L)$ and $A(\nu_S)$ for the excitation and scattered field, and a chemical SERS effect, described by an increased Raman cross section σ_{ads}^R of the adsorbed molecule compared to the cross section in a “normal” Raman experiment σ^R . N is the number of molecules involved in the SERS process. The graph was taken from reference [45].

SERS is typically used for capturing and identifying specific signal for ultrasensitive detection of unknown species and for imaging by creating SERS “tags”. For example, flower-like silver mesoparticles with highly roughened surfaces were used as SERS substrates.[52] The structures were functionalized with dye molecules, and high and reproducible SERS enhancements in the order of 10^7 – 10^8 on average could be achieved. As a result, the detection limitation could reach the single molecule level. In another case, silver NPs were functionalized with dye molecules as SERS tags for in vivo cancer imaging.[53] The excitation wavelength was chosen in the NIR range, and then the penetration depth reached up to a few centimeters. By this method, small tumors could be identified and located noninvasively using a Raman system.

1.3.2 Surface Enhanced Fluorescence

Fluorescence is the emission of light by matter induced by absorption of EM radiation (Figure 1.7).[54] The wavelength of emission is generally longer than the absorbed radiation wavelength.

In some special cases, a pair of photons with same or different energy could be absorbed by one electron when the incident EM radiation is intense; this can lead to emission of a shorter wavelength, which is called “two-photon absorption”.[55] The wavelength of emission may also be the same as that of the absorbed radiation, termed "resonance fluorescence".

Fluorescence emission and Raman scattering are two different and competing phenomena, with the major differences being the nature of intermediate states and the time scale involved in these processes (Figure 1.8). As mentioned in previous sections, in the Raman scattering, generally virtual states are involved, while in fluorescence real states are concerned. The existence of such virtual states explains why in Raman scattering, the interaction of the photon with the molecule and the re-emission of scattered photon occur almost simultaneously ($<10^{-12}$ s, picosecond), while the lifetime in fluorescence is longer ($>10^{-9}$ s, nanosecond).

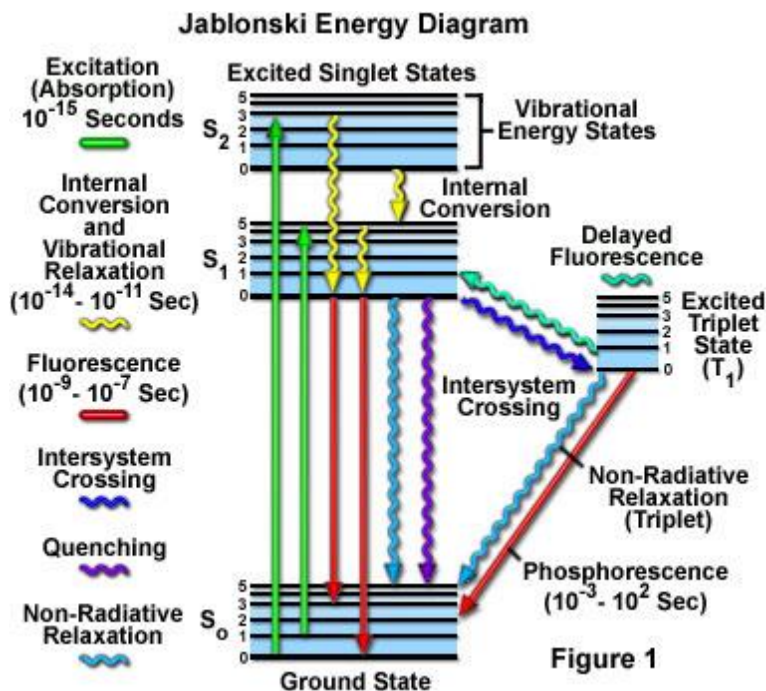


Figure 1.7 Jablonski diagram. After an electron absorbs a high energy photon the system is excited electronically and vibrationally. The system relaxes vibrationally, and eventually fluoresces at a longer wavelength. The graph was taken from internet. <http://www.olympusmicro.com/primer/techniques/fluorescence/fluorescenceintro.html>

When the energy of excitation photon gets close to the transition energy between two electronic states, resonance Raman or resonance fluorescence will happen. In contrast with resonant fluorescence, relaxed fluorescence is the emission of a photon from the lowest vibrational level

of an excited electronic state. When the excitation energy is lower, fluorescence could not take place and only off-resonance Raman scattering could be excited. However, in resonance excitation, the fluorescence is much more intense than Raman scattering and general hiding Raman features, because the fluorescence scattering cross section is 10^{-17} – 10^{-16} cm² per molecule, much larger than that of Raman 10^{-30} – 10^{-25} cm² per molecule.[45] For this reason, when searching for the more informative Raman spectrum, the fluorescence should be avoided, for example, select the longer excitation wavelength.

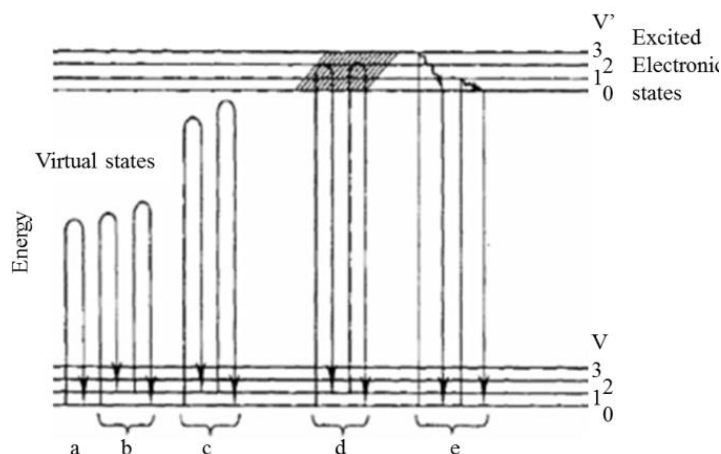


Figure 1.8 Mechanisms of various light scattering processes. (a) Rayleigh, (b) nonresonance Raman, (c) pre-resonance Raman, (d) resonance Raman resonance fluorescence (e) relaxed fluorescence. The graph was taken from the website of Horiba Scientific. <http://www.azom.com/article.aspx?ArticleID=2950>

Ultraviolet (UV)-excited fluorescence in the Vis region has led to many practical applications including photodetectors, fluorescent labeling, dyes, light-emitting diodes, biosensors and solar cells.[56-58] Although fluorescence has relatively large cross sections, there is still a driving force for faster detection, enhanced intensity and higher signal-to-noise ratios. Recently, metallic nanostructures were used to modify the spectral properties of fluorophores and to alleviate some of these photophysical constraints.[59-63] When fluorophores are located in the vicinity of metallic nanostructures, the photoluminescence (PL) could be enhanced. It is called surface enhanced fluorescence (SEF).[26, 64-67] SEF occurs due to fluorophores' interaction with metallic nanostructures, which result in modifications of their excitation/emission activities.[41, 57, 68-70] The strength of these interactions depends on the overlap degree of SPR with the absorption/emission of fluorophores, and the distance between metal and fluorophores.[71, 72]

The plasmon/fluorophore interactions lead to three effects: excitation enhancement (amplified excitation light that leads to an enhanced absorption), emission enhancement (increased radiative decay thus an amplification of emission) and quenching (increased nonradiative decay).[58, 66, 70, 72, 73] In general, for the excitation enhancement mechanism, the PL intensity is directly proportional to the EM field enhancement $|E|^2$. [6, 73] For the emission enhancement mechanism, radiative rate could be increased and thereby the lifetime and quantum yield are modified. Quenching occurs when the distance between metal and fluorophores is smaller than ~ 5 nm, so the coupling distances should be controlled at ≥ 5 nm. [33, 74] Overall, the final performance is determined by the competition between enhancement and quenching effects. EFs vary from 2 to 100, which depend on the particular plasmon/fluorophore system. [6, 69] SEF can be used to increase detection sensitivity. For example, colloidal semiconductor quantum dots (QDs) were assembled between layers of metal NPs to create a highly strong plasmon-exciton interaction in the plasmonic cavity. [75] In such a plasmon/fluorophore system, Ozel, *et al* observed an EF of 4.4 and a shortened decay lifetime. Such strong plasmon-exciton coupling nanocomposites hold great promise for future exploitation and development of QD plasmonic biophotonics and QD plasmonic optoelectronics. [75]

1.3.3 Optical Detection of the Change in Refractive Index

Optical properties have been largely exploited for biological labeling and diagnostic applications. [76, 77] One of the simplest applications in this branch is to detect the change of environmental refractive index through measuring the shift of SPR peak location, which is quite sensitive to the variation of the refractive index of the local environments. [7, 9, 10, 78]. When refractive index changes, the wavelength of SPR peak shifts follow an approximately linear relationship. The SPR sensitivity (S) is reported as nanometers of peak shift (λ_p) per refractive index unit (nm RIU^{-1}). [9, 79]

$$S = \frac{d\lambda_p}{dn} \tag{5}$$

The sensitivity achieves the highest value at the wavelength and the angle of incident light, which could satisfy the resonance condition. In general, nanostructures are first dispersed in solution directly or immobilized on glass substrates and inserted into solution later, and then the

extinction or scattering spectra are measured. By monitoring the peak shift, the variation of the refractive index of the solution could be measured. The precision of the sensitivity is described as a figure of merit (FOM) which is defined by the sensitivity and the resonance line width.[9]

$$FOM = S/\Delta\lambda \quad (6)$$

Many noble metal nanostructures, such as gold nanorods in solution,[42] silver nanorice structures immobilized on glass slips[80] or dispersed in solution[35, 81], nanoholes and nanohole arrays,[10] have been used for this purpose. The size, shape, composition, and inter-particle spacing could affect the detection sensitivity.[8] For example, when the end curvature, the aspect ratio of 1D nanostructures and the size uniformity increase, the SPR sensitivity increases.[42, 81] In addition, the capping agents, which have been used during the synthesis process also play an important role in this application. When the surface of nanostructures is functionalized with capture molecules, target molecules can be detected as their binding with capture molecules alters the dielectric environment near of the surface that can be monitored by the shift of SPR.[6]

1.4 Synthesis of Silver Nanostructures

1.4.1 Unique Properties of Silver Nanostructures

Nobel metals offer many advantages for plasmonic applications with respect to other plasmonic metals.[82] First, the frequency of SPRs is at the desired region, i.e., the Vis to NIR range. If the excitation frequency is lower than that of metal's SPR, the light will be reflected. Unlike most metals, whose SPR frequency is in the UV range and are shiny in the Vis range, noble metal such as Au,[15] Ag,[6, 33] and Cu,[83] yield strong SPR in the Vis-NIR region, resulting in strong absorption and showing special colors. In particular, silver is able to exhibit a strong SPR tunable over a wavelength range of 300 to 1200 nm, wider than that of most plasmonic metals.[6] In addition, comparing with gold, silver has sharper resonances, higher refractive index sensitivity, and is less dissipative.[16, 23, 84] More importantly, silver is also a good candidate for SPP applications with respect to other metals, such as Au and Al, because it possesses the lowest absorption in the Vis region with typical SPP propagation distance ranging from 10-100 μm at a

Ag/air interface. Moreover, the chemical stability of silver can be improved by forming a silver sulfide thin film on the surface to prevent oxidation.[6]

1.4.2 Synthesis of Silver Nanostructures

The size and shape of nanostructures have a critical effect on the frequency, bandwidth and intensity of LSPR.[17, 33] The ability to control such physical parameters of silver nanostructures and further to maneuver their plasmonic properties are important for practical application. A lot of investigations have been focused on the size-controlled[85] and shape-controlled[86] wet chemical synthesis of silver nanostructures in the last two decades, and the development of nanofabrication techniques allow the manipulation of nanostructure geometries and assemblies using another approach. Wet chemical procedures involve the reduction of metal precursors to metal atoms, and the controlled aggregation of atoms into nanostructures. In general, the wet-chemistry approach, such as the citrate reduction method, polyol method, has proved to be a reproducible, high-yield, large-scale synthesis method to obtain Ag nanostructures with excellent optical properties.[23] As shown in Table 1.1, many silver nanostructures could be obtained from wet chemical methods. For example, the size of silver nanocubes was tuned from 30-70 nm by introducing a trace amount of sulfide or hydrosulfide into reaction solution and by switching silver precursors.[87] It was further tailored in the range of 18-32 nm by quenching the reaction at different times.[88] In addition to the size control, the geometry of silver nanostructures could also be adjusted.[21] Shapes like spheres,[23, 89] cubes,[87] icosahedra,[90] triangular nanoprisms,[91] bars,[92] nanorice structures,[92, 93] rods[94] and wires[16] could all be synthesized by wet chemical methods. In the following, we focused our brief discussion on several wet chemical methods.

Citrate reduction is a popular method for quickly synthesizing silver colloids, which was first reported in 1982.[95] In this method, AgNO_3 is used as a precursor and citrate is used as both reducing agent and a stabilizer. Silver NPs could be obtained by adding certain amounts of aqueous sodium citrate solution into silver nitrate aqueous solution under boiling. This method is feasible but it is hard to control the shape and size.[96, 97] A large variety of sizes and a diversity of shapes of the products make fundamental studies rather complicated and also limit their practical applications.

Table 1.1 Summary of the Shapes, LSPR Absorption Peaks, Demonstrated Applications, and Methods for the Synthesis of Ag Nanostructures

Shape	Illustration	LSPR ^a	Applications ^b	Method of Synthesis
Sphere and quasi-sphere		320 - 450	SERS; LSPR sensing; assembly	Polyol process (single-crystal); Citrate reduction (quasi-sphere)
Cube and truncated cube		400 - 480	SERS; LSPR sensing; assembly	Polyol process; Seed-mediated growth
Tetrahedron and truncated tetrahedron		350 - 450	SERS	Polyol process; Light-mediated Growth
Octahedron and truncated octahedron		400 - 500	Assembly	Polyol process; seed-mediated growth; light-mediated growth
Bar		350 - 900	SERS	Polyol process
Spheroid		350 - 900	SERS	Polyol process
Right bipyramid		500 - 700	-	Polyol process
Beam		-	Electron transport	Polyol process
Decahedron		350 - 450	-	Seed-mediated growth; light-mediated growth; citrate reduction
Wire and rod		380 - 460	Wave guiding; electronics; SERS; assembly	Seed-mediated growth
Polygonal plates and disc		350 - 1000	SERS; LSPR sensing	Light-mediated growth; polyol process
Branched structures		400 - 1100	SERS	Seed-mediated growth
Hollow structures		380 - 800	SERS; LSPR sensing	Template-directed growth

^a The main absorption peak (nm). ^b Assembly means the nanostructure has been assembled into larger structures for plasmonic applications or studies. The red lines in the illustration refer to a crystalline plane; the dark faces are {100}, and the light faces are {111}. The table was taken from reference [6].

The silver mirror reaction is a chemical deposition method used to form Ag coating on various types of substrates.[98] In this approach, AgNO₃ is used as a precursor to form the Tollen's reagent, a sugar or an aldehyde-containing compound is used as reducing agent to generate elemental Ag. The silver mirror reaction could generate a shiny coating made of small

particles,[99] leaf or flowerlike fractal structures[98] of Ag on objects, but no shape control has been reported with this technique.

Polyol process that has been widely used in the controlled synthesis of silver nanostructures is a robust and versatile method.[6] Polyols are compounds with multiple hydroxyl functional groups available for reactions. By varying reaction conditions, such as reaction temperature, reaction time, capping agent, reagent concentration and trace ions, the nucleation and further growth process could be highly controlled to obtain nanostructures with different morphology and size.[20, 100] A number of morphologies synthesized through this method are listed in Table 1.1 and further shown in Figure 1.9.

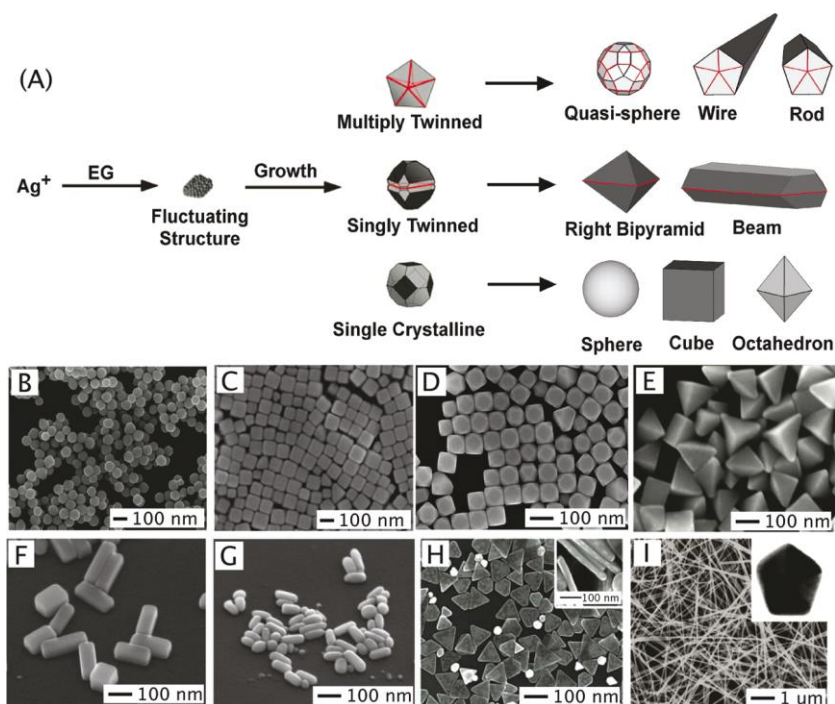


Figure 1.9 Polyol method for synthesizing Ag nanostructures. In (A) the reduction of Ag ions by EG leads to the formation of nuclei that are highly volatile. As the nuclei grow, fluctuations cease and their structure becomes static and contains multiply twinned boundary defects, singly twinned boundary defects, or are single crystalline with no boundary defects. These seeds are then grown into different nanostructures like (B) spheres, (C) cubes, (D) truncated cubes, (E) right bipyramids, (F) bars, (G) spheroids, (H) triangular plates, and (I) wires. The red lines in the illustration refer to a twin plane; the dark faces are {100}, and the light faces are {111}. The graph was taken from reference [6].

In polyol method, AgNO_3 or CF_3COOAg are used as precursors, with the first one being more commonly used. However, CF_3COOAg -involved synthesis has some unique features that could be beneficial for the preparation of certain structures, such as a lower reaction temperature,

higher stability, and insensitivity to trace impurities. Polyol reagents, such as ethylene glycol (EG), polyethylene glycol (PEG), 1,2-propylene glycol, or 1,5-pentanediol can serve as both solvents and reducing agents.[23] The reduction happens when Ag precursors and capping agents are mixed in the presence of polyols, especially at an elevated temperature. The capping agents are generally used to stabilize the particle and play a role as shape control through selectively binding the facets of nanocrystal. At the beginning, silver ions are reduced as atoms to form small clusters of fluctuating structures. With the reaction continuing, the clusters grow larger and form more stable structures, such as single crystalline, singly twinned and multiply twinned nanocrystals, which then act as seeds. The seeds with different inner structures ultimately develop into the nanostructures of different morphologies.[6]

1.5 Thesis Objectives and Organization

1.5.1 Our Objectives

Part I: Synthesis

Although some Ag nanostructures have been synthesized with tunable size and shape as mentioned above, it is challenging to synthesize uniform Ag nanorice structures with high reproducibility. The growth mechanism of such nanostructures is not well understood and the knowledge on key shape determining parameters also remains limited. The ability to understand these aspects can potentially lead to better control over the reproducibility, shape uniformity, and yield on the shape-directed synthesis of these nanorice structures. In addition, their optical properties require further investigation before they can be explored for practical applications. Moreover, although some 1D Ag nanostructures have been fabricated from solution, nearly all of them are highly symmetric. This feature is attributed to the crystal symmetry in face centered cubic (FCC) structure, which inhibits asymmetric growth.[22] Rare examples of asymmetric 1D nanostructures have been reported, such as Cu nanobats,[83] rod-needle and plate-belt Ag hetero-nanostructures[101] and tadpole-shaped Au nanowires.[102] However, a detailed analysis of the plasmonic properties of these asymmetric nanostructures is lacking. The controlled preparation of asymmetric silver nanostructures with well-defined SPR peaks using a simple solution synthesis method is thus desirable for creating novel platforms for exploring morphology-dependent optical properties, but remains a significant challenge. Given these gaps

in synthesis and understanding, in the Part I, we further investigated the growth process of the silver nanorice and nanocarrot structures.[103] The optical properties of these silver nanostructures were further examined. The objectives for Part I are:

1. Studying the growth mechanism of silver nanorice structures. By understanding the growth mechanism, further optimizing and gaining more control over the synthesis to achieve adjustable silver nanostructures by changing the reaction parameters.
2. Synthesizing novel asymmetric silver nanocarrot structures and corresponding structure/property relationship characterization. In addition, the growth mechanism will be investigated.
3. Analyzing the plasmonic properties of both structures in detail by optical extinction spectroscopy and electron energy-loss spectroscopy (EELS).
4. Measuring the sensitivity of both structures to the refractive index of their environments.

Part II: Investigation of Potential Applications

Surface enhanced spectroscopy (such as SERS and SEF) is one of these popular plasmonic applications of silver nanostructures. For these applications, the substrates and excitation wavelength are critical factors that influence the observed enhancement. Vis and NIR radiations are usually used to excite SPR modes of silver nanostructures to provide maximal enhancement. As for metal substrates, the EM field intensity distribution around them is not uniform and depends strongly on their morphology. Structures with sharp surface curvatures and tips[52] (in prisms[8] or rods [38]) and junctions[104] (in core/shell structures[39] or dimers[8]) can produce large EM enhancement. Further to achieve the strong coupling between plasmons of adjacent nanostructures, the distance below several nanometers is desired, but hard to control. Such gaps or junctions usually rely on the random assembly of small particles. Although a number of researches have focused on the applications based on the concept of surface enhanced spectroscopy, the production of reliable, reproducible, and highly sensitive substrates for sensing applications has been a big challenge.

Individual flower-like silver mesoparticles with rough surface have excellent performance in SERS.[52] The SERS EFs of dimers were 10-100 times larger than that of individual particles, which were further confirmed by our experiments. Such increases in SERS could arise from the

additional field enhancement in the interparticle gaps. The study of the enhancement mechanism and manipulation of the formation of dimers is necessary for SERS applications.[105]

SEF of colloidal QDs has drawn plentiful attentions recently. Among all kinds of QDs, lead chalcogenide QDs have both large excitation Bohr radii and small bulk band gaps, thus allowing quantum confinement in relatively large sized QDs simultaneously with a tunable NIR emission.[56, 57, 106] The intricate behaviour of plasmon/fluorophore interaction require extensive investigations to understand and control the relative contributions of the light absorption enhancement and alterations of both radiative and nonradiative decay rates, all these being crucial for the advancement of theoretical investigations and for practical applications. We focused on the PL enhancement in the plasmon/fluorophore system consisting of lead chalcogenide QDs and Ag NP film to investigate the interaction between QDs and plasmonic structures. Ag NPs instead of Ag “nanorice” or “nanocarrot” structures were used here because the high stability of NPs makes it easier to claim the concept for completing the preliminary work.

Therefore, the objectives for Part II are:

1. Investigating the incident polarization-dependent SERS of flower-like silver mesoparticle dimers and manipulating individual particles to form or break the dimers in order to investigate the enhancement mechanism *in situ*.
2. Fabricating coupled plasmon/fluorophore system consisting of lead chalcogenide QDs and Ag NP film and investigating the PL enhancement. By controlling the range of spectral superposition between the absorption/emission spectra of the QDs and the SPR of the Ag films, the enhancement mechanism will be studied.

1.5.2 Organization of the Thesis

This thesis is divided into four chapters and organized as follows:

Chapter 1 Introduction: introducing the background, motivation and objectives of this thesis.

Chapter 2 Experimental, Characterization and Theoretical Modeling: describing experiment details of synthesis processes of all kinds of silver nanostructures and QDs involved in the current study, investigating the potential applications in refractive index sensitivity and surface

enhance spectroscopy and introducing the main characterization techniques and the theoretical modeling methods.

Chapter 3 Results:

Part I: Synthesis

Section I: Silver Nanorice Structures: Oriented Attachment-Dominated Growth, High Environmental Sensitivity, and Real-Space Visualization of Multipolar Resonances

Section II: Asymmetric Silver “Nanocarrot” Structures: Solution Synthesis and their Asymmetric Plasmonic Resonances

Part II: Investigation of Potential Applications

Section III: Enormous Surface Enhanced Raman Scattering from Dimers of Flower-like Silver Mesoparticle

Section IV: Photoluminescence Enhancement of Near-infrared Emitting PbS and PbS/CdS Core/shell Quantum Dots Induced by Silver Nanoparticle Film

Chapter 4 Conclusions and Perspectives: Concluding the main results and perspecting some potential investigations in future work.

Most of work in this thesis was done by Hongyan Liang, however, some parts were conducted through collaboration. More specifically, the EELS measurements and corresponding calculations were performed by Dr. David Rossouw working in our collaborator Prof. Gianluigi A. Botton’s group. All QDs used in this thesis were provided by Dr. Haiguang Zhao, who also assisted with me for PL intensity and lifetime measurements. All Mie calculations were modeled by Prof. Zhipeng Li. The FDTD modeling was performed by Dr. Scott K. Cushing in our collaborator Prof. Wu’s group.

CHAPTER 2 EXPERIMENTAL, CHARACTERIZATION AND THEORETICAL MODELING

In this chapter, experiment details for the synthesis, characterization and modeling of four kinds of silver nanostructures and QDs, and for the preparation of samples for investigating the effect of the refractive index on SPR and surface enhanced spectroscopy were described. Firstly, silver nanorice structures, nanocarrot structures, flower-like silver mesoparticles, nanospheres and QDs were synthesized. Then, silver nanorice structures and silver nanocarrot structures were used to study the SPR shifts with the change of refractive index. Flower-like silver mesoparticles were used for SERS applications. Furthermore, silver NPs were combined with QDs for investigating SEF. At last, all characterization methods used to investigating the morphology, structure, composition and optical properties as well as the theory methods were introduced.

2.1 Materials

AgNO₃ (99.8%), silver trifluoroacetate (CF₃COOAg), NaSH, poly(vinyl pyrrolidone) (PVP) with an average molecular weight of 40,000 (PVP K30), ascorbic acid, lead (II) chloride (98%), sulfur (100%), oleylamine (OLA) (amine content, >98 wt%; C₁₈-amine content, 70 wt%), cadmium oxide (99%), oleic acid (OA), octadecene (ODE), tetrahydrofuran (THF), 3-aminopropyltrimethoxysilane, EG, polymethylmethacrylate (PMMA), nitric acid (HNO₃), hydrochloride acid (HCl), malachite green isothiocyanate (MGITC) were obtained from Sigma-Aldrich Inc. PEG 600 was purchased from Xilong Chemical Industry Incorporated Co. LTD. Hexane, toluene, chloroform, dimethyl sulfoxide, and ethanol were purchased from Fisher Scientific Company. All chemicals were used as purchased. All air and water-sensitive chemicals were kept in the glove box under the protection of N₂. Deionized water with resistance of 18 MΩ·cm was used in all the cases.

2.2 Synthesis of Silver Nanostructures

Schematic illustration of the typical reaction setup for silver nanostructures solution preparation was shown as below (Figure 2.1). A round-bottom flask was immersed in an oil bath for reaction.

The thermometer was inserted in the oil bath for monitoring temperature. A stirring bar was put in the reaction solution for continuously stirring. In the following, all the silver nanostructures were synthesized by using this reaction setup.

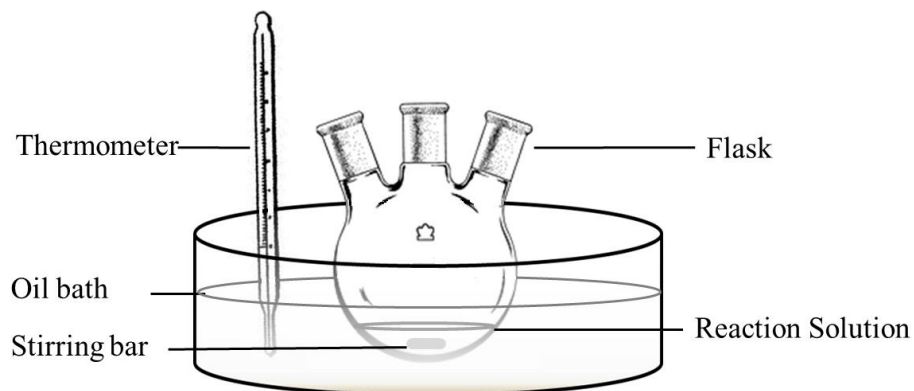


Figure 2.1 Schematic illustration of the setup for Ag nanostructures preparation.

2.2.1 Silver Nanorice Structures

The silver nanorice structures were synthesized via a polyol approach.[80] For a typical synthesis, the stock solution had to be prepared in advance. Firstly, 1.11g PVP was dissolved in 100 mL of PEG 600 under stirring at room temperature. The concentration of PVP was calculated in terms of the repeating units and the final concentration of PVP is 100 mM. Secondly, 0.338 g AgNO_3 was dissolved in 1 mL of deionized water to form aqueous precursor solution with a concentration of 2M. 1 mL of 2 M AgNO_3 aqueous solution was added to the PEG/PVP mixture. The solution was allowed to incubate at room temperature for at least one month. 15 mL of stock solution was put in a 100 mL of flask, and then was heated to and kept at 70 °C in an oil bath for ~2 h (stage I). The reaction solution showed a yellow color at the beginning of the reaction and then the color faded. When the yellow color disappeared, the nearly-colorless solution was further heated at 100 °C for growth (stage II). During the stage II, the reaction solution went through a series of color changes. The light yellow reappeared after the solution was heated at 100 °C, then the color became dark and turned to green. With time increasing, the green color became dark and a grey color showed. After 12-14 h, silver nanorice structures could be obtained in a grey colloidal solution. No intentional control over the atmosphere was exerted in these operations.

For the growth mechanism studying, the reaction was performed under the same or the modified reaction condition. At various time intervals, aliquots of the reaction mixture were taken from the reaction solution by a glass pipette and quenched by cold water to room temperature for immediate absorption measurements or for other characterizations after product purification. To minimize the temperature perturbation during sampling, the glass pipet was preheated for 20s by suspending it above the reaction solution before it was immersed into the reaction solution.

In order to examine the effect of oxygen on the synthesis of the silver nanocrystals, the reaction was also performed under the protection of N₂ for comparison. Two different conditions were applied. In one scenario, 15 mL of the stock solution was firstly bubbled with N₂ under vigorous stirring for 30 min and then vacuumed for 20 min. In this way, the oxygen in the reaction solution was expected to expel. After that, the synthesis followed the above described procedures (stages I and II) with the only exception being under N₂. In the other scenario, the reaction of stage I was followed the typical process. At the beginning of stage II, the nearly-colorless reaction solution was bubbled with N₂ under vigorous stirring for 30 min and then vacuumed for 20 min. Finally, the N₂ protection was applied to the full process of stage II.

The product was purified by centrifugation at 11,000 rpm for 20 min after adding certain amount of acetone. The transparent supernatant was removed and the precipitates were then dispersed in deionized water or ethanol by ultrasonic. The centrifugation process was repeated for four times to remove excess PEG 600 and PVP. Finally, the sample was dispersed in ethanol for further characterization.

2.2.2 Silver Nanocarrot Structures

The silver nanocarrot structures were also synthesized via a polyol approach, and the silver nanocarrot structures were obtained by reducing CF₃COOAg with PEG 600 under the surface protection of PVP at high temperature. In a typical synthesis, 0.222g PVP K30 was dissolved into 20 mL PEG 600 in a flask under continuously stirring at room temperature. The final concentration of PVP which was calculated in terms of the repeating units was 100 mM. After that, 0.4 mL of 1M CF₃COOAg aqueous solution was added to the mixture and then the flask was heated at 95 °C in an oil bath for ~18 h under stirring. No intentional control over the atmosphere was exerted in these operations. The reaction solution was quenched by placing the

reaction flask in air at room temperature. During the growth process, the color of solution changed with time, similar as that described in the synthesis of silver nanorice structures. At the beginning, the reaction solution was light yellow after the silver precursor was added. With time increasing, the yellow color disappeared and reappeared again, which went through a series of color changes, from yellow to green and then grey. For growth mechanism investigation, aliquots of the reaction mixture were taken from the reaction solution by a glass pipette at various time intervals and quenched by cold water to room temperature for immediate absorption measurements or for other characterizations after product purification. To minimize the temperature perturbation during sampling, the glass pipet was preheated for 20 s by suspending it above the reaction solution before it was immersed into the reaction solution. The product was purified by centrifugation at 11,000 rpm for 10 min after adding certain amounts of acetone. The transparent supernatant was removed and the precipitates were then dispersed in ethanol by ultrasonic. The samples were washed with ethanol for four times to remove excess PVP, the remaining precursor and PEG 600. Finally, the silver nanocarrot structures were dispersed into ethanol for further characterization.

2.2.3 Flower-like Silver Mesoparticles

The flower-like silver mesoparticles were obtained by reducing AgNO_3 with ascorbic acid under the protection of capping agent.[52] In a typical synthesis, a AgNO_3 aqueous solution (0.3 mL, 1 M) and a PVP K30 (2 mL, 0.1 M) aqueous solution were added to deionized water (10 mL) in a flask with a magnetic stirrer at room temperature. The concentration of PVP was calculated in the terms of the repeating units. An ascorbic acid (0.2 mL, 1 M) aqueous solution was then quickly injected into the vigorously stirred mixture. The solution became grey immediately and then changed to dark grey a few minutes later, which indicated the appearance of a large quantity of colloidal silver particles. By this procedure, colloidal silver flower-like mesoparticles with a radius of about 1 μm can be obtained. The nearly-smooth, quasi-spherical silver mesoparticles were synthesized via a similar process, with the modification of the quantity of AgNO_3 , ascorbic acid and PVP, and the additional introduction of a HNO_3 aqueous solution (0.05 mL, 15 M). A sample of the silver particles was obtained by centrifugation and was washed with ethanol several times to remove the excess surfactant.

2.2.4 Silver Nanospheres

The nanospheres with the SPR peak at 420 nm (Ag#1) were synthesized via a polyol approach reported by Xia, *et al.*[107] Typically, EG (5 mL) was added into a 50 mL round bottom flask and heated under magnetic stirring at 150 °C. NaSH (60 μ L; 3 mM in EG) was quickly injected into the heated solution. Two minutes later, a 3 mM HCl solution (0.5 mL) was injected into the heated reaction solution, followed by the addition of PVP (1.25 mL, 20 mg/mL in EG). After another 2 min, CF₃COOAg (0.4 mL, 282 mM in EG) was added into the mixture. The reaction time was 10 min. The reaction solution was quenched by placing the reaction flask in an ice-water bath. All the samples were collected by centrifugation and then washed with acetone once and then alcohol four times to remove the remaining precursor, EG and excess PVP. Finally, the Ag NPs were dispersed into ethanol for further investigation.

The nanospheres with the SPR peak at 450 nm (Ag#2) were synthesized via polyol approach by using PEG as solvent and reduction agent modified from reported protocol.[80, 89, 93] In a typical synthesis, PVP (1.11g) was dissolved in 100 mL of PEG under stirring, followed by the addition of 1 mL of 2 M AgNO₃ aqueous solution. Then the solution was heated to and kept at 70 °C in an oil bath for ~2 h. When the yellow color disappeared, the nearly-colorless solution was further heated at 80 °C for 16h. All the samples were collected by centrifugation and then washed with acetone once and then alcohol four times to remove the remaining precursor, EG and excess PVP. Finally, the Ag NPs were dispersed into ethanol for further investigation.

2.3 Synthesis of Quantum Dots

The schematic illustration of the typical reaction setup for QDs preparation is shown as below. (Figure 2.2) Since the QDs are very sensitive to oxygen, the synthesis was performed under N₂ atmosphere. A round-bottom flask was inserted in oil bath for reaction. The thermometer was inserted in reaction solution directly for monitoring temperature. A stirring bar was put in reaction solution for continuously stirring. In the following, all the QDs were synthesized by using this reaction setup.

Note that all QDs used in this thesis were provided by Dr. Haiguang Zhao.

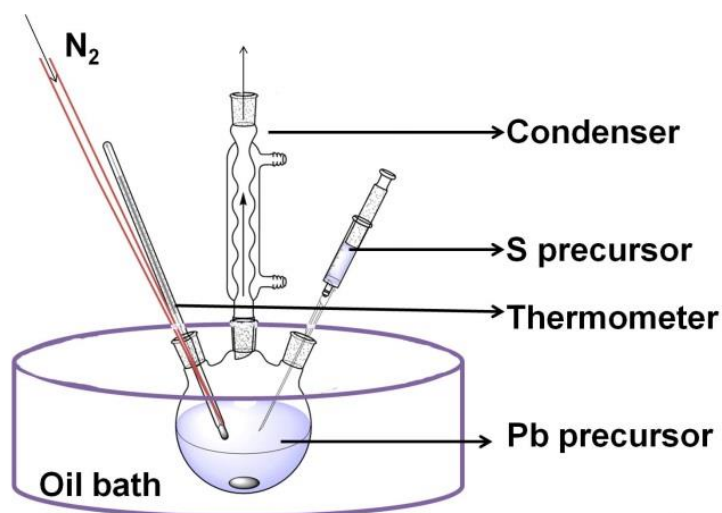


Figure 2.2 Schematic illustration of the air-free reaction setup for synthesizing QDs.

2.3.1 PbS Quantum Dots

PbS QDs were synthesized by using OLA as ligands in a simple, “non-viscous”, solventless, constant-temperature reaction system and a relatively safe precursor S.[108] Typically, PbCl_2 (3.6 mM) in OLA (2.4 mL) and sulfur (0.36 mM) in OLA (0.24 mL) were purged, respectively, by N_2 at room temperature for 30 min. The PbCl_2 -OLA suspension was then heated to 160 °C and kept at this temperature for 1 hour. Subsequently, the PbCl_2 -OLA suspension was cooled to 120 °C under vacuum for 15 min. The flask was then reopened and the N_2 flux was restored. Sulfur in OLA at room temperature was quickly injected into the PbCl_2 -OLA suspension under vigorous stirring. The growth reaction was conducted at 100 °C for 1–360 min to obtain PbS QDs of different sizes and then the reaction cell was quenched with cold water. For purification, alcohol was added into cold reaction solution, and then the solution was centrifuged and supernatant was removed. The QDs were re-dispersed in toluene or chloroform.

2.3.2 PbS/CdS Quantum Dots

Recent studies have revealed that the core/shell structure can stabilize and maximize the fluorescence of core QDs. Cation exchange approach is an efficient way to produce the core/shell structure of QDs. Herein, the thin-shell PbS/CdS QDs (the shell thickness is about 0.7 nm) were achieved by cation exchange method [60], as shown in Figure 2.3.

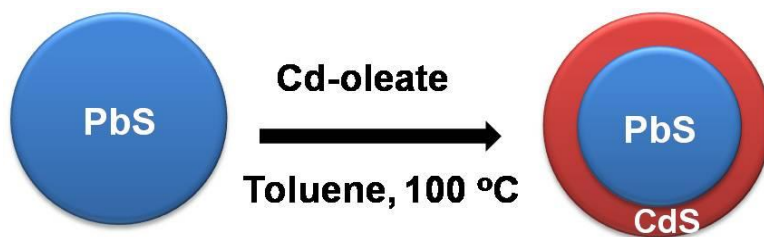


Figure 2.3 Schematic illustration of the synthesis of thin-shell PbS/CdS QDs by cation exchange.

The cation exchange procedure was carried out under N_2 atmosphere. All solvents used in the procedure are anhydrous and oxygen free. PbS QDs were synthesized by using OLA ligands as mentioned before. The procedure is as follows: CdO (2.3 mM), OA (2 mL) and ODE (10 mL) were heated to 255 °C under N_2 protection for 20 min. The clear solution was cooled to 155 °C under vacuum for 15 min. The flask was then reopened and the N_2 flux was restored. PbS QD suspension in toluene (1 mL, absorbance = 3 at the first excitation peak) was diluted in 10 mL toluene, bubbled for 30 min in N_2 and then heated to 100 °C immediately. The Cd/OA mixture was injected into the PbS QD suspension. The reaction cell was quenched with cold water after the growth reaction was conducted at 100 °C for different time. For purification, alcohol was added to quenched reaction solution, and then the suspension was centrifuged and supernatant was removed. Finally, the QDs were dispersed in toluene or chloroform for further investigation. The general synthesis process can produce the PbS/CdS QDs with first-exciton peak wavelength spanning from 1100 to 1500 nm by choosing different, initial PbS sizes and varying the reaction time and molar ratio of PbS QD to Cd-oleate.

2.4 Preparation of Sample for Studying Refractive Index Effect

2.4.1 Preparation of A Monolayer of Silver Nanorice Structures

A silver nanorice structure monolayer was deposited on a (3-aminopropyl) trimethoxysilane-coated glass substrate by exposing it to the diluted nanorice structure alcohol solution for 2 h. Then, the substrate was rinsed by alcohol and dried by N_2 . The SPR sensitivity of the nanorice structures was studied by immersing the monolayer of isolated nanorice structures immobilized on a glass slide into solvents with different refractive index and monitoring the variation of their

UV-Vis-NIR spectra. The plasmon shift was plotted as a function of the refractive index, which was linearly fitted to determine the sensitivity of the SPR to the refractive index.

2.4.2 Preparation of Silver Nanocarrot Structure Solution

Silver nanocarrot structures were dispersed into the ethanol-PEG600 mixture to investigate the response of SPR peaks to the refractive index of surrounding medium. The ethanol-PEG 600 volume ratios were varied to change the refractive index of the surrounding medium. The volume percentage of PEG 600 in the liquid mixture was varied from 20% to 100% at a step of 20%. Extinction spectra of the solutions including silver nanocarrot structures were measured. The plasmon shift was plotted as a function of the refractive index, which was linearly fitted to determine the sensitivity of the SPR to the refractive index.

2.5 Preparation of Samples for Surface Enhance Spectroscopy

2.5.1 Preparation of Samples for Surface Enhance Raman Scattering

Samples for SERS measurements were prepared following procedures below: MGITC molecules solution (0.1 mL, 10^{-6} M) was mixed with the same volume of silver suspension. The corresponding concentration of the silver mesoparticles in the suspension was estimated to be about 10^{-12} M and this means that there were of the order of 10^6 MGITC molecules per silver particle. The high density of MGITC solution could ensure that there were some molecules reside in the junctions between two particles. The mixed solution was allowed to incubate overnight to achieve a high adsorption of MGITC molecules on the surface of particles. The excess of free MGITC molecules in the supernatant were removed after centrifugation at 3000 rpm for 3 min. The precipitate was dispersed in ethanol. Through this process, monolayer of MGITC molecules was left on the surface of the particles, although the presence of multilayers cannot be absolutely excluded, especially on the surface of crevices. Further, one drop of the solution containing silver particles was spin-coated on a clean Si slide, and then rinsed with ethanol to remove unabsorbed particles and dried under a stream of N_2 . Subsequently, the Si slide was decorated with an indexed TEM grid consisting of $100 \mu\text{m} \times 100 \mu\text{m}$ grids, which facilitated *post situ* both the optical and SEM imaging of desired particles. All post-deposition experiments were performed on the air-Si interface.

2.5.2 Preparation of Ag NP/QD Films for Surface Enhanced Fluorescence

Firstly, we attached two batches of Ag NPs with different resonance features (SPR peak located at ~420 nm and ~450 nm) to 3-aminopropyltrimethoxysilane-treated glass slides by a drop-casting approach. A monolayer of Ag NPs could be obtained; however, multilayers may also exist. Then the formed Ag NP film was over-coated a thin layer of PMMA via spin coating (0.5% PMMA in chloroform, 3000 RPM, 1 min). After that the PbS or PbS/CdS QDs suspended in chloroform with 0.5% PMMA were further coated on the top of PMMA film via spin coating (two steps: 1500 RPM, 5s and then 2500 PRM, 40s).

2.6 Studying Morphology, Crystal Structure and Composition

Characterization methods for structure, composition and property were introduced herein.

2.6.1 Scanning Electron Microscopy

SEM is a type of electron microscope, which is generally used to directly observe the morphology and size of nanostructures.[109, 110] When the focused beam of electrons interacts with the electrons in the sample, various signals containing the surface topography and composition information could be produced for detection. These types of signals are secondary electrons, back-scattered electrons, X-rays, cathodoluminescence, specimen current and transmitted electrons. The highest resolution could reach even one nanometer. SEM images of silver nanostructures were obtained using a HITACHI S-4800 SEM. To perform these measurements, all samples were washed first to remove the excess surfactant and then dispersed in ethanol solution. After that, a drop of ethanol solution containing nanocrystals was deposited onto silicon or ITO glass slides (both of them are conductive) and dried in air. The shape of nanostructures could be observed clearly under SEM. For size estimation, the dimensions of about 100 particles in SEM images were measured.

2.6.2 Transmission Electron Microscopy and Selected Area Electron Diffraction

TEM allows the direct visualization of nanostructures and has been a typical tool for observing their morphology, size and structure.[111, 112] In this technique, the electron beam can transmit

through an ultra-thin specimen and interact with it to generate some signal for characterization. Under a high voltage electron beam, the nanostructures give high contrast to the background. Under certain circumstances, resolution can reach the sub-angstrom level, which is normally referred to as high resolution TEM (HRTEM). HRTEM can provide the information about crystal structures via atomic spacing and crystalline direction measurements. With the help of selected area electron diffraction (SAED), crystal structures can be identified. In current work, to perform these measurements, a drop of ethanol solution containing nanocrystals was deposited onto a Cu grid coated with thin (5 - 50 nm in thickness) carbon films. The grid was subsequently dried in air before being introduced into TEM. The SAED pattern and HRTEM were measured at different locations on the sample with a JEOL 2100F microscope. The average size of particles was estimated by measuring the dimensions of about 100 particles in TEM images.

2.6.3 Energy Dispersive X-ray Spectroscopy

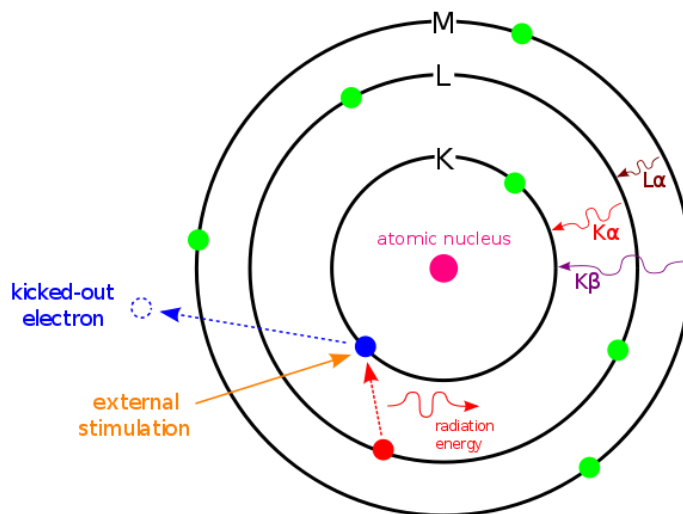


Figure 2.4 Schematic illustration of EDX. The graph was taken from internet. <http://commons.wikimedia.org/wiki/File:EDX-scheme.svg>

Energy dispersive X-ray spectroscopy (EDS) is a technique used for determining the elemental composition of a material. As atomic structures are different for different elements, the X-ray spectrum of each element is unique. When the high-energy beam of charged particles is focused on a sample, the ground state electron could be excited while creating a hole in the inner shell. To fill the hole, an electron with higher energy from an outer shell will jump and release the excess energy in the form of an X-ray. In our experiment, the EDS system is an atmospheric thin

window detector from Oxford Instrument Company with a resolution of 133eV. This detector is equipped in SEM and controlled by the “Link ISIS” software. In this thesis, it was used to measure the number and energy of X-ray emitted and further identifies elements in specimens.

2.6.4 Powder X-ray Diffraction

Powder X-ray diffraction (XRD) is one of the most common non-destructive methods used for determining the crystal structure of a solid specimen, in which the crystalline structures cause a beam of X-rays to diffract into crystallographically specific directions with different intensities.[113, 114] In a powder sample, the orientation of each grain is random and overall the specimen is isotropic. Using XRD, phase and crystalline domain size can be decided. Herein the XRD study of silver nanocrystals was carried out with a Philips X’pert diffractometer using Cu K_{α} radiation source ($\lambda = 0.15418$ nm). During measurements a grazing incidence angle of 5 °with step size of 0.1 °and counting time of 15 seconds per step was used. In order to perform XRD measurements, highly concentrated particle solution was deposited on silicon or glass substrate, and dried in air to form a film.

2.7 Studying Optical Properties

2.7.1 Electron Energy-Loss Spectroscopy

When a beam of electrons with a very narrow range of kinetic energies is focused on a specimen, some of the electrons will undergo inelastic scattering, losing energy and deflecting their initial path.[115, 116] Through measuring the amount of energy loss via an electron spectrometer, physical processes related to different energy losses can be probed.[117] In our case, EELS was used to investigate the excitation of plasmons.

EELS measurements were performed on an FEI Titan 80-300 TEM equipped with an electron monochromator and a Gatan Tridiem 865 spectrometer. Samples were prepared by placing a drop of the nanocrystal solution onto a silicon nitride TEM membrane (Norcada). The TEM was operated at 80 keV in both parallel illumination and scanning probe modes. EELS spectra were recorded on a charge-coupled device camera (256×2048 pixels) at an energy dispersion of 0.01 eV per channel with an exposure time of 2 ms per spectrum. The spectral resolution was 90 meV

as measured by the full width at half maximum of zero loss peaks. During data acquisition, a focused electron probe was rastered over rectangular two dimension region of interest enclosing an individual structure. At each position in the raster, high and low angle electron scattering intensity was collected simultaneously, carrying structural information in the annular dark field (ADF) image and spectral information in the EELS signals, respectively. This configuration enables the precise spatial correlation of the spectroscopic data in EELS imaging and the geometric data in ADF image. As a result, relevant information on peak energies and intensities of SPR modes of each spectrum can be selected and analyzed from any position in the two dimension scan with nanometer precision.

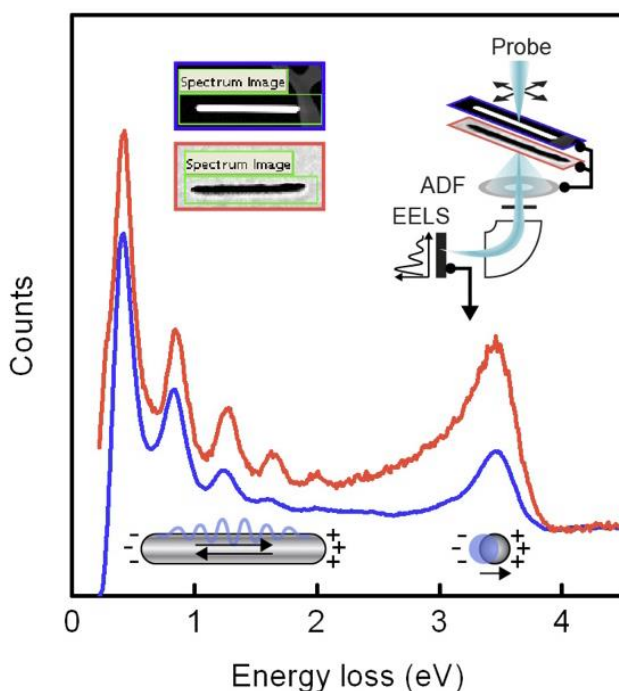


Figure 2.5 The nanoscale spectroscopy of a silver nanowire (blue) and nanoslot (red) probed by EELS (insert on the right). The graph was taken from reference [37].

The EELS measurements in this thesis were performed by Dr. David Rossouw working in our collaborator Prof. Gianluigi A. Botton's group.

2.7.2 Extinction Spectroscopy

UV-Vis-NIR spectroscopy is a useful technique to monitor the SPR.[118] Herein a UV-Vis-NIR spectrophotometer (Varian Cary 5000) was used to measure extinction spectra using a scan

speed of 600 nm/min. All experiments were done in a transmission mode on liquid samples in the Vis and/or NIR range. A reference was used to obtain a baseline before each experiment.

2.7.3 Raman Spectroscopy

Raman signal was measured with a Renishaw inVia micro-Raman spectroscopy system. Samples were excited with a 632.8 nm HeNe laser at low power (in the μW range under the objective) to minimize heating and photochemical effects. The laser was blocked by a 633 nm edge filter.

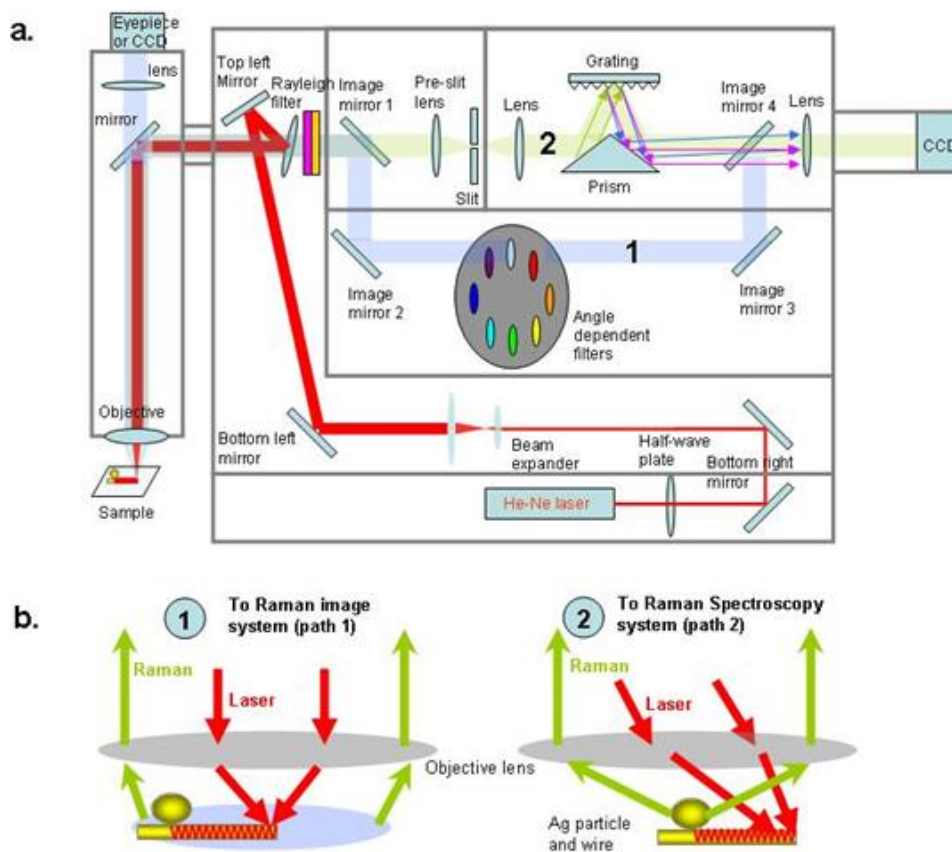


Figure 2.6

a, Schematic illustration of the confocal Raman system. The optical path 1 is for the Raman imaging, and the optical path 2 is for the measurement of Raman spectra. b, Sketches for Raman image and spectra acquisition. When using the image function, mirrors 1&4 are moved into the optical path, and the optical path 2 is thus blocked. The laser is focused on one end of the Ag wire through an objective; the Raman signals from the sample are collected by the same objective. After passing the Rayleigh filter, the optical signals go through an angle dependent narrow band pass filter, which permits one Raman peak ($\pm 20 \text{ cm}^{-1}$) pass, and arrive at the TE air cooled 576×400 CCD to produce an image. To acquire remote Raman spectra, mirrors 1 & 4 should be moved out of the path, and the confocal Raman spectral acquisition mode marked with path 2 is then used for collecting Raman spectra with the same CCD. The top left, bottom left and bottom right mirrors need to be adjusted to move the laser focus point to the position for plasmon excitation, e.g. one end of the Ag nanowire. The graph was taken from reference [28].

Incident polarization was tuned by a half wave plate in order to effectively excite randomly oriented dimers. The sample was mounted on an XY stage of a Leica microscope, equipped with a 100× (NA = 0.95) objective which was used for excitation and collection, and the spot size is around 1 μm in diameter. Raman images were taken using the air cooled 576 × 400 CCD array in a confocal Raman system with a spectroscopic window width of ± 20 cm⁻¹, while the unfocused laser light spread all over the measured area. The Raman spectra were collected in the backscattering geometry by the same CCD.

A micromanipulator (MMO-202ND, Narishige) equipped on an optical microscope was used to form or break the dimers controllably for SERS measurements.

2.7.4 Steady-state and Time-resolved Photoluminescence Spectroscopy

The fluorescence spectra of QDs were taken from a Fluorolog®-3 system (Horiba Jobin Yvon). The xenon lamp or lasers were used to excite the QDs. PL lifetime of QDs was measured using a pulsed laser diode and fast multichannel scaler mode in the Fluorolog®-3 system. QY measurements for PbS or PbS/CdS QDs were performed using Dye IR 125 dissolved in dimethyl sulfoxide as a reference. In our experiments, the decay signals were found to be best fitted to a two-exponential function, according to the following equation:

$$I(t)/I_0 = A_1 \exp(-t/\tau_1) + A_2 \exp(-t/\tau_2) \quad (1)$$

where τ_1 and τ_2 are lifetime components, I is PL intensity, t is time and I_0 is the initial PL intensity at $t = 0$. A_1 and A_2 values are the fractional contribution of each of two components. Intensity-weighted average lifetime values reported were calculated using the various fit components as follows:

$$t_{\text{(average)}} = (a_1 \tau_1^2 + a_2 \tau_2^2) / (a_1 \tau_1 + a_2 \tau_2) \quad (2)$$

Where τ_1 and τ_2 are the lifetime of QDs and a is the percentage of each lifetime component.

The PL intensity and lifetime measurements were assisted with Dr. Haiguang Zhao.

2.8 Theory

Theoretical modeling methods are listed as below:

2.8.1 Mie Theory

To evaluate the EM enhancement effect of the flower-like silver mesoparticles or NPs, we applied the generalized Mie calculation. For the simulation of flower-like silver mesoparticle dimers, the silver mesosphere diameter used in our calculation was set to be 1 μm , and the gap distance between two particles was set to be 3 nm based on the size of ascorbic acid and MGITC molecules on the surface. The multipoles were taken up to 50, which was enough for the convergence of the simulation. To estimate the scattering of coupled NPs at different separating distance, we also applied the generalized Mie calculation to a pair of silver nanospheres separated at 1, 2, 5, 10 nm. The diameters of spheres were set at 100 nm and 50 nm.

These Mie calculations were modeled by our collaborator Prof. Zhipeng Li.

2.8.2 Finite-Difference Time-Domain Simulation

Theoretical modeling of the optical extinction spectrum of an individual silver nanocorrot structure was performed by using the FDTD method in the commercially available Optiwave software FDTD 10.0. The Ag nanocorrot was replicated using a three dimensional wedge structure and the size was reproduced using the average size from TEM measurements. The refractive index of silver was fit by the model of reference.[119] The simulation cell used a linearly polarized Gaussian input pulse and perfectly absorbing boundary conditions with a grid size of half a nanometer. The polarizations were tested to replicate the random orientation in actual experiments. Two polarizations were adjusted to excite transverse or longitudinal modes. The FDTD modeling was performed by Dr. Scott K. Cushing in our collaboration Prof. Wu's group.

2.8.3 Boundary Element Method

Calculations of the electron energy loss probability for 1D nanostructures at resonance were done according to solutions of Maxwell's equations using the BEM, implemented with the MNPBEM Matlab toolbox. The toolbox computes the external potentials associated with a specified electron beam trajectory required for BEM calculations such that the boundary conditions of Maxwell's equations in the quasistatic approximation are fulfilled. The

nanostructure dimensions used for these calculations were the same as those in the EELS experiments and the simulated particle was comprised of 1924 faces.

The BEM calculations in this thesis were performed by Dr. David Rossouw working in our collaborator Prof. Gianluigi A. Botton's group.

CHAPTER 3 RESULTS

3.1 Part I: Synthesis

It is introduced in Chapter 1 that 1D silver nanostructures draw worldwide attentions due to the possibility of systematically controlling their size and shape in synthesis and thereby tuning their LSPR, as well as applying them to a series of important applications, such as catalysis and biological labeling. Generally, 1D nanostructures support transverse and longitudinal SPR modes. When the aspect ratio increases, the longitudinal SPR red shifts and higher order multipolar SPR modes will appear. Although a lot of 1D silver nanostructures have been reported, such as nanowires,[23] nanorods,[16] nanorice structures and nanobars,[92, 93] reports on the well-controlled, high-yield synthesis of novel 1D silver nanostructures and on corresponding investigation of their structure and plasmonic properties are still rather limited. In this part, the development of two structures, silver nanorice structures and silver nanocarrot structures is described. Both of silver nanostructures were achieved through a polyol approach, and the setup and methods for synthesis were shown in Chapter 2. Focuses were placed on optimizing the experimental conditions and studying the growth mechanism of the 1D silver nanostructures. At the same time, the optical properties were characterized by different techniques as introduced in Chapter 3. The effect of the change of surrounding refractive index on the shift of SPR peak location was also studied.

Part I is divided into two sections, each corresponding to a publication focusing on one type of nanostructure. In Section I, we focused on studying the growth mechanism of silver nanorice structures and optimizing the experimental conditions. In Section II, we focused on the synthesizing asymmetric silver nanocarrot structures and corresponding characterization of its crystal structures and optical properties. In the following, both publications are preceded by a brief description of the reasons that motivated the experimental work.

Section I Silver Nanorice Structures: Oriented Attachment-Dominated Growth, High Environmental Sensitivity and Real-Space Visualization of Multipolar Resonances

Hongyan Liang, Haiguang Zhao, David Rossouw, Wenzhong Wang, Hongxing Xu, Gianluigi A. Botton, and Dongling Ma

Chem. Mater., 2012, 24, 2339.

While silver nanorice structures have been synthesized before,[93] the growth mechanism is still not clear and the understanding on key shape-determining parameters remains very limited. Moreover, the reproducibility of synthesis yet needs to be significantly improved. The main difference of morphology between silver nanorice structures and nanorods is that nanorice structures have sharp tips, which could affect the plasmonic properties. However, the optical properties of these novel nanorice structures also require further investigations. Moreover, it is desirable yet challenging to image the plasmonic resonance in the spatial domain in order to provide insights into the light-matter interactions at the nanometer scale and understand if these nanostructures behave qualitatively differently from more simple nanostructures.

Given these gaps in information and understanding, in the present section, we investigated the growth process of the silver nanorice structures. It was found that the seed selection process, based on the oxidative etching of the twinned crystals, was an indispensable step for the growth of the nanorice structures and oxygen played a critical role in this seed selection process. The major shape development stage of the nanorice structures was dominated by the oriented attachment along the $\langle 111 \rangle$ direction. Increasing reaction temperature could lead to dramatic change in the growth mechanism and morphology of nanostructures. The longitudinal SPR of the nanorice structures was found to be highly sensitive to the refractive index of surrounding dielectric media, which made them highly promising for sensor applications. Furthermore, in addition to the longitudinal resonance, the multipolar resonances in individual nanorice structures were mapped in real space by using high-resolution EELS technique.

Cet article a dû être retiré en raison de restrictions liées au droit d'auteur.

Vous pouvez le consulter à l'adresse suivante :

DOI : 10.1021/cm3006875

Supporting information

Silver Nanorice Structures: Oriented Attachment-Dominated Growth, High Environmental Sensitivity and Real-Space Visualization of Multipolar Resonances

**Hongyan Liang,[†] Haiguang Zhao,[†] David Rossouw,[‡] Wenzhong Wang,[‡] Hongxing Xu,^{*,§}
Gianluigi A. Botton,[‡] and Dongling Ma^{*,†}**

[†] INRS-Énergie, Matériaux et Télécommunications, Université du Québec, 1650 Boulevard
Lionel-Boulet, Varennes (QC), J3X 1S2, Canada

[‡] Department of Materials Science and Engineering, McMaster University, 1280 Main Street W.
Hamilton ON, L8S 4L7, Canada

[‡] School of Science, Minzu University of China, Beijing 100081, P. R. China

[§] Institute of Physics, Chinese Academy of Sciences, Beijing 100190, P. R. China, and Division
of Solid State Physics, Lund University, Lund, 22100, Sweden

E-mail: hongxingxu@aphy.iphy.ac.cn; ma@emt.inrs.ca

Supporting figures

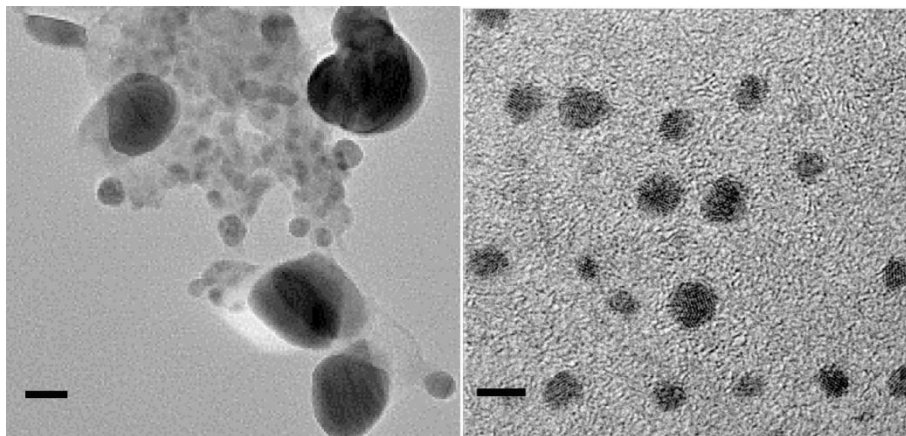


Figure S1. The TEM image (left) of silver NPs synthesized at 100 °C for the total reaction time of 4 h. The right is the HRTEM image of the smaller NPs. Scale bar for left is 20 nm and for right is 4 nm.

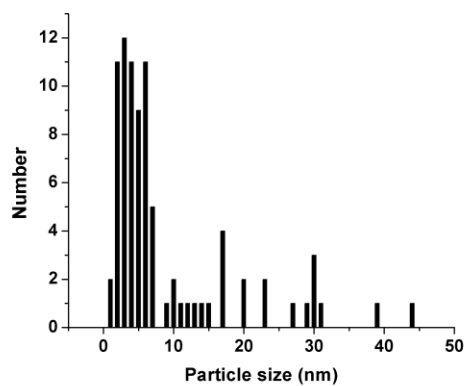


Figure S2. The size distribution of silver NPs at stock solution.

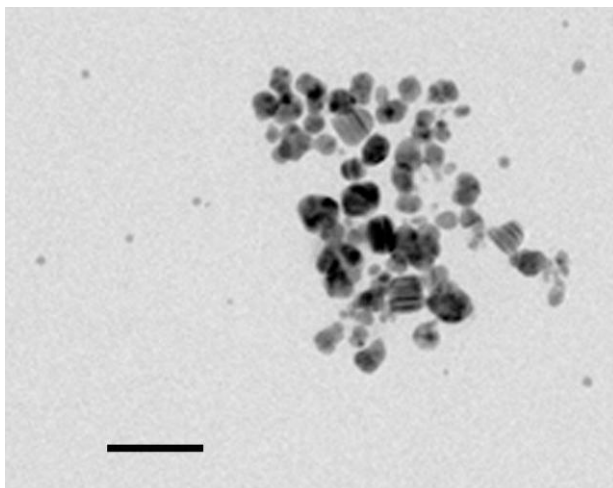


Figure S3. The TEM image of silver NPs taken from the oxygen-free reaction at 100 °C for the total reaction time of 5 h. Scale bar is 50 nm.

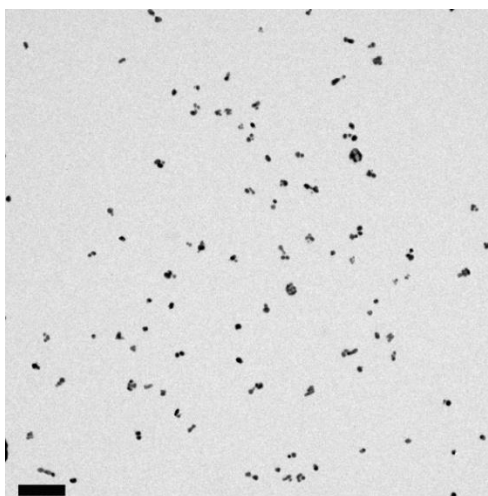


Figure S4. The TEM image of silver NPs synthesized at 100 °C for the total reaction time of 4.5 h. Scale bar is 200 nm.

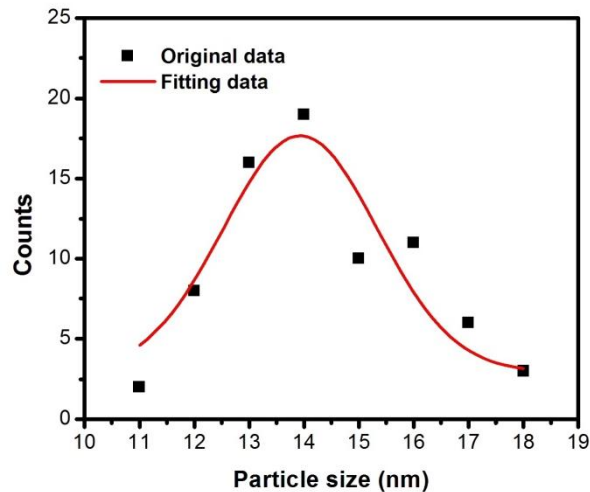


Figure S5. Size distribution of silver NPs (not include the attached silver NPs) synthesized at 100 °C for the total reaction time of 4.5 h (13.9 ± 2.8 nm).

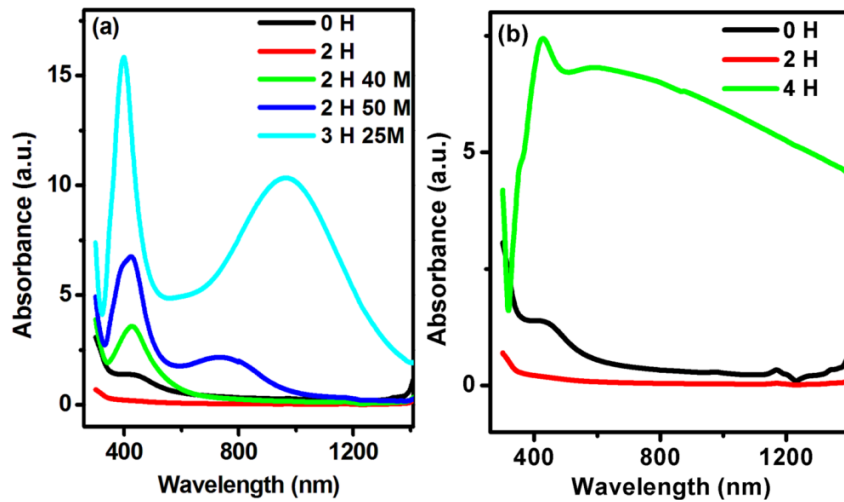


Figure S6. UV-Vis-NIR spectra of the samples synthesized at 120 °C (a), and 160 °C (b).

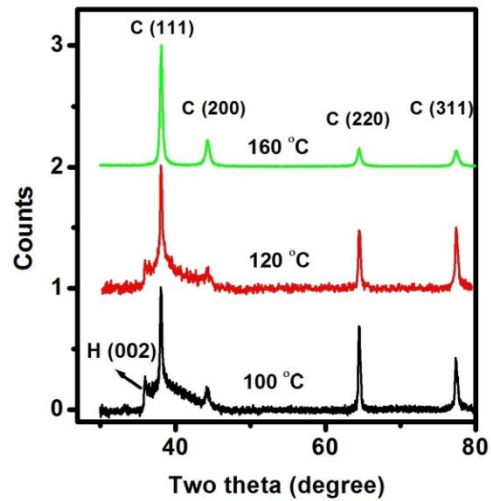


Figure S7. XRD patterns of the samples synthesized at 100 °C, 120 °C and 160 °C, respectively. C denotes FCC diffraction and H denotes HCP diffraction.

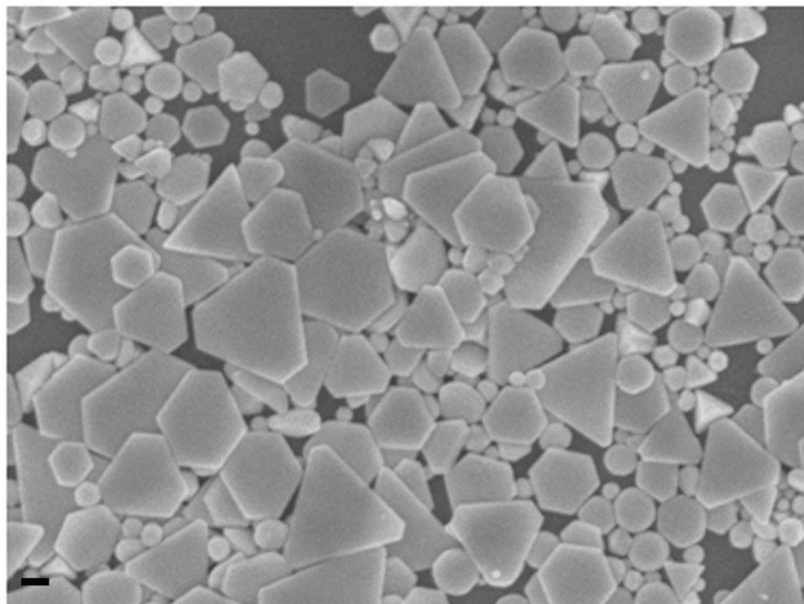


Figure S8. The SEM image of silver nanoplates synthesized at 160 °C with total reaction time of 4 h. The yield of silver nanoplates relative to the total number of silver nanocrystals formed was optimum estimated to be higher than ~50%. Scale bar is 100 nm.

Section II Asymmetric Silver “Nanocarrot” Structures: Solution Synthesis and Their Asymmetric Plasmonic Resonances

Hongyan Liang, David Rossouw, Haiguang Zhao, Scott K. Cushing, Honglong Shi, Andreas Korinek, Hongxing Xu, Federico Rosei, Wenzhong Wang, Nianqiang Wu, Gianluigi A. Botton and Dongling Ma.

J. Am. Chem. Soc., 2013, 135, 9616.

Investigations of 1D nanostructures have so far been focused on symmetric structures, such as the nanorice structures mentioned in the previous section. The reports on asymmetric structures remain very limited, perhaps partially due to the fact that the crystal symmetry in the FCC structure typically leads to the formation of the symmetric 1D silver nanostructures. The optical properties of asymmetric 1D structure also require further investigations. Moreover, it is desirable yet challenging to image the plasmonic resonance in the spatial domain in order to provide insights into the light-matter interactions at the nanometer scale and understand if these nanostructures behave qualitatively differently from more simple nanostructures or symmetric 1D nanostructures.

Given these gaps in lack of information and understanding, in the present section, we investigated the synthesis, SPR properties and structure/property relationship of novel silver nanocarrot structures synthesized at high yield for the first time. Silver nanocarrot structures were achieved through a polyol approach. The method was modified from the one in Section I,[80, 93] and the main difference was that CF_3COOAg was involved as precursor instead of AgNO_3 . The crystals exhibited mixed twins and stacking fault domains along the $\langle 111 \rangle$ longitudinal direction. Oriented attachment was the dominated mechanism for anisotropic growth. Multipolar plasmon resonances up to fourth order were measured by optical extinction spectroscopy and EELS and were in agreement with theoretical calculations. Compared to symmetric 1D nanostructures of similar length, the dipole modes in the nanocarrot structures showed a clear redshift. Due to the asymmetric morphology, EELS maps showed an asymmetric distribution of the resonant plasmonic fields in the nanocarrot and a compression of the resonance node spacing towards the tail, significantly different from the symmetric distribution in 1D symmetric structure, which was shown in Section I. In addition, by increasing the length of the nanocarrot structures, the intensity of the longitudinal SPR peaks increased, accompanied by

the steady redshift of the peaks. In particular, a strong longitudinal resonance at 1717 nm was achieved for the nanocarrot structures with the average length of 250 nm. Such a long wavelength resonance was rare in silver nanostructures obtained from solution synthesis. Silver nanocarrot structures also showed a high sensitivity of $890 \pm 87 \text{ nm RIU}^{-1}$ (RIU, refractive index unit) to the refractive index of their environment.

Cet article a dû être retiré en raison de restrictions liées au droit d'auteur.

Vous pouvez le consulter à l'adresse suivante :

DOI : [10.1021/ja404345s](https://doi.org/10.1021/ja404345s)

Cet article a dû être retiré en raison de restrictions liées au droit d'auteur.

Vous pouvez le consulter à l'adresse suivante :

DOI : 10.1021/ja404345s

Asymmetric Silver “Nanocarrot” Structures: Solution Synthesis and Their Asymmetric Plasmonic Resonances

Hongyan Liang,[†] David Rossouw,[‡] Haiguang Zhao,[†] Scott K. Cushing,[§] Honglong Shi,^{||} Andreas Korinek,[‡] Hongxing Xu,[⊥] Federico Rosei,[†] Wenzhong Wang,^{||} Nianqiang Wu,[§] Gianluigi A. Botton,[‡] and Dongling Ma^{*,†}

[†]INRS-EMT, Université du Québec, 1650 Boul. Lionel-Boulet, Varennes, QC, Canada J3X 1S2

[‡]Department of Materials Science and Engineering, McMaster University, 1280 Main Street West, Hamilton, ON, Canada L8S 4L7

[§]Department of Mechanical & Aerospace Engineerings, West Virginia University, Morgantown, West Virginia 26506, United States

^{||}School of Science, Minzu University of China, Beijing 100081, P. R. China

[⊥]Institute of Physics, Chinese Academy of Sciences, Beijing 100190, P. R. China

Methods.

Synthesis of Silver Nanocarrot. In a typical synthesis, 0.4 mL of 1M CF₃COOAg aqueous solution and 0.222 g poly(vinyl pyrrolidone) (PVP) with an average molecular weight of 40,000 were added to 20 mL polyethylene glycol 600 (PEG 600) in a flask and then the flask was heated at 95 °C in an oil bath for ~18 h under continuously stirring. The final concentration of CF₃COOAg and PVP (in terms of its repeating units) was 20 mM and 100 mM, respectively. The average length of the product from this synthesis condition is 200 ± 31 nm. By modifying the parameters, the length could be tuned and the details are shown in Table S1. The samples were collected by centrifugation and then washed with acetone once to remove the remaining precursor and PEG 600 and then with alcohol four times to remove excess PVP. The silver nanocarrots were dispersed into alcohol for further characterization.

Characterized of Silver Nanocarrot.

Low- and high-resolution transmission electron microscopy (TEM) micrographs were obtained with a JEOL 2100F microscope. Nanocarrots' sizes were estimated by measuring the dimensions of about 100 particles in TEM images. The powder X-ray diffraction (XRD) study of silver nanocrystals after extensive purification was carried out with a Philips X'pert

3.2 Part II: Investigation of Potential Applications

Sensing based on the concept of surface enhanced spectroscopy is one popular plasmonic application for silver nanostructures, as introduced in Chapter 1. Although a lot of research has focused on these investigations, the production of reliable, reproducible, highly sensitive substrates for sensing applications is still a big challenge. Towards realizing such applications, SERS and SEF based on silver nanostructures were investigated in this Part. All synthesis processes were shown in Chapter 2 and all characterization methods were introduced in Chapter 3. Part II is divided into two sections, corresponding to investigation of SERS and SEF, respectively. In Section III, we focused on investigating the incident polarization-dependent SERS of flower-like silver mesoparticle dimers and manipulating individual particles to form or break the dimer in order to investigate the enhancement mechanism *in situ*. In Section IV, we focused on fabricating coupled plasmon/fluorophore system consisting of lead chalcogenide QDs and Ag NPs and investigating PL enhancement. By adjusting the level of spectral superposition between the absorption/emission spectra of the QDs and the SPR of the Ag films, the optical performance of QDs was modified and the enhancement mechanism was investigated.

In the following, two manuscripts reporting SERS and SEF, respectively, are preceded by a brief description of the reasons that motivated the experimental work.

Section III Enormous Surface Enhanced Raman Scattering from Dimers of Flower-like Silver Mesoparticle

Hongyan Liang, Zhipeng Li, Zhuoxian Wang, Wenzhong Wang, Federico Rosei, Dongling Ma and Hongxing Xu

Small, 2012, 8, 3400.

SERS is a powerful and extremely sensitive spectroscopic tool, which can provide spectral fingerprint of molecules up to the single molecule level. However, it has been very challenging to form SERS substrates with high SERS enhancement and large area of “hot spots”. In the present work, we used the method of micro-manipulation to create flower-like silver mesoparticle dimers, and found that the huge SERS EF (about 7 orders of magnitude on single flower-like mesoparticles due to the highly rough surfaces) was further increased by 10~100 times through forming dimers. The strong SERS dependence of the dimers on the incident polarization revealed that the significant additional SERS enhancement was caused by the SPs coupling effect in the dimers. Moreover, the protrusions on one roughened particle could be merged to the grooves on the other roughened particle in dimers to create an extremely large “hot spot” area of the micrometer size at the junction of two particles that favors SERS dramatically. In contrast, the “hot spot” area in a dimer of smooth spheres with the same size as roughened particles is only about tens of nanometers. Moreover, the use of the micro-manipulation allowed us to achieve dimers with high SERS enhancement controllably and reproducibly.[105]

Cet article a dû être retiré en raison de restrictions liées au droit d’auteur.

Vous pouvez le consulter à l'adresse suivante :

DOI : 10.1002/smll.201201081

NANO MICRO
small

Supporting Information

for *Small*, DOI: 10.1002/smll.201201081

**Enormous Surface-Enhanced Raman Scattering from Dimers
of Flower-Like Silver Mesoparticles**

*Hongyan Liang, Zhipeng Li, Zhuoxian Wang, Wenzhong
Wang, Federico Rosei, Dongling Ma, and Hongxing Xu **

Photoluminescence Enhancement of Near-infrared Emitting PbS and PbS/CdS Core/shell Quantum Dots Induced by Silver Nanoparticle Film

H.Y. Liang,^a H.G. Zhao,^a Z.P. Li,^b C. Harnagea,^a and D.L. Ma^a

^a Institut National de la Recherche Scientifique, University of Québec, 1650 Boulevard Lionel-Boulet, Varennes, Québec, J3X 1S2 Canada

^b Beijing Key Laboratory of Nano-Photonics and Nano-Structure (NPNS), Department of Physics, Capital Normal University, Beijing, 100048 China

E-mail: zhaoh@emt.inrs.ca and ma@emt.inrs.ca

Table S1 Emission peak position(nm) and QY of investigated PbS and PbS/CdS core/shell QDs measured in toluene.

Samples	λ_{em} (nm)	QY (%)
PbS#1	1100	85
PbS#2	1320	40
PbS#3	1400	26
PbS#4	1500	19
PbS/CdS#1	1190	52
PbS/CdS#2	1350	49
PbS/CdS#3	1460	36

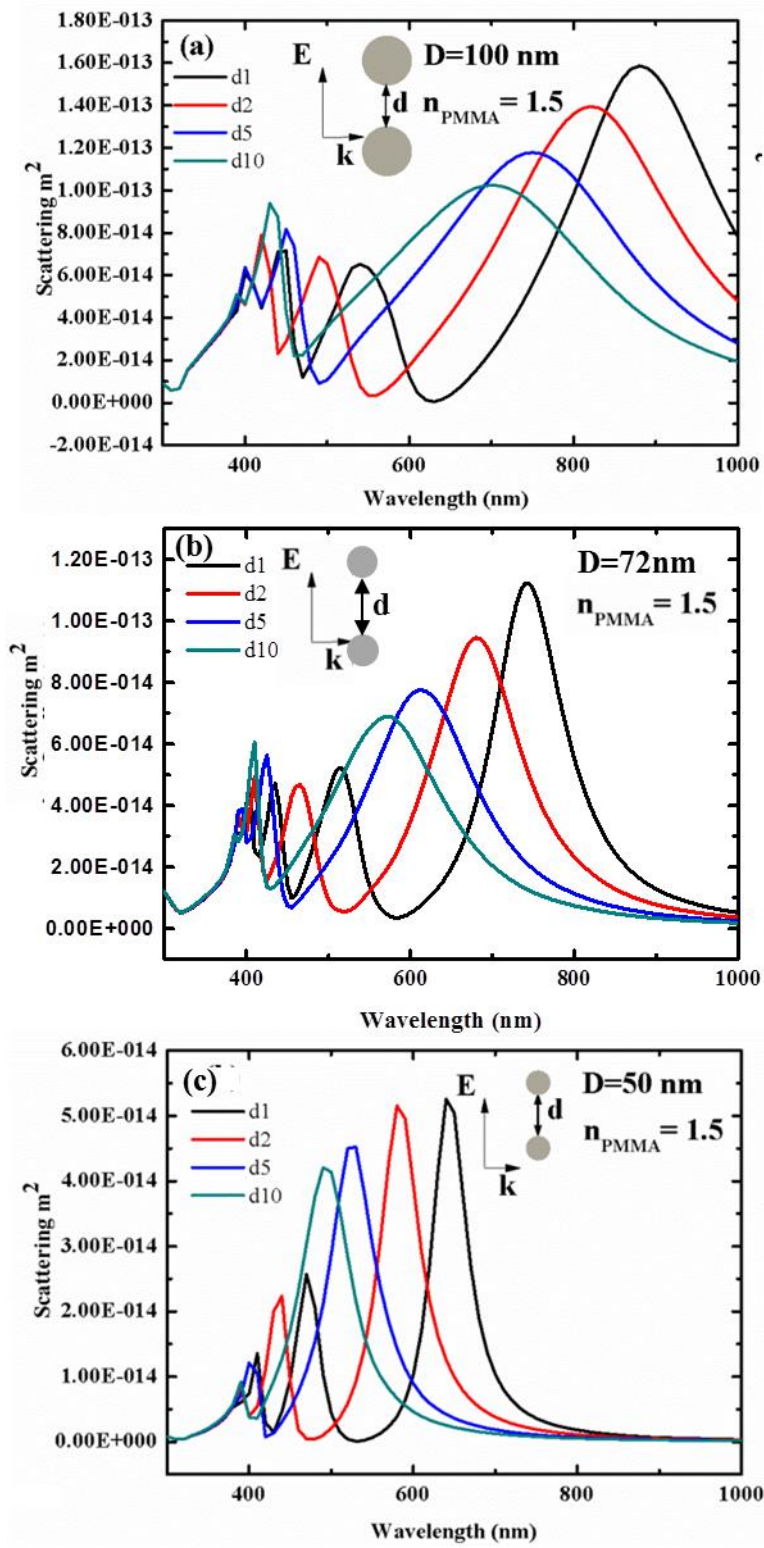


Figure S1. Calculation of the scattering by coupled spheres at different separation distances: $d=1, 2, 5, 10$ nm. The diameters of spheres are 100 nm in (a), 72 nm in (b) and 50 nm in (c).

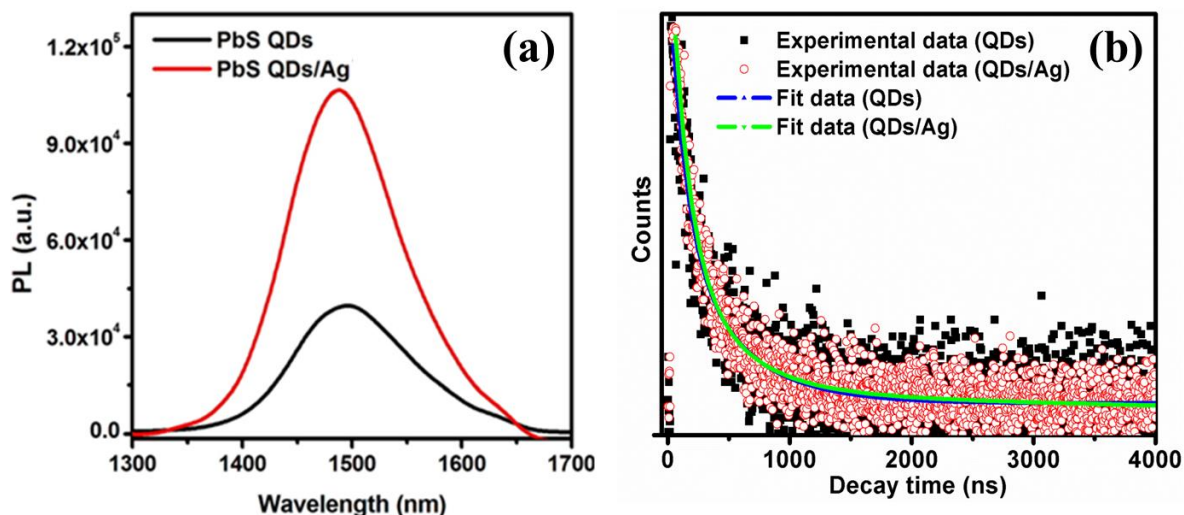


Figure S2. Typical PL spectra (a) under 450 nm excitation and PL decay curves (b) under 444 nm excitation of PbS QDs with and without the presence of Ag#1.

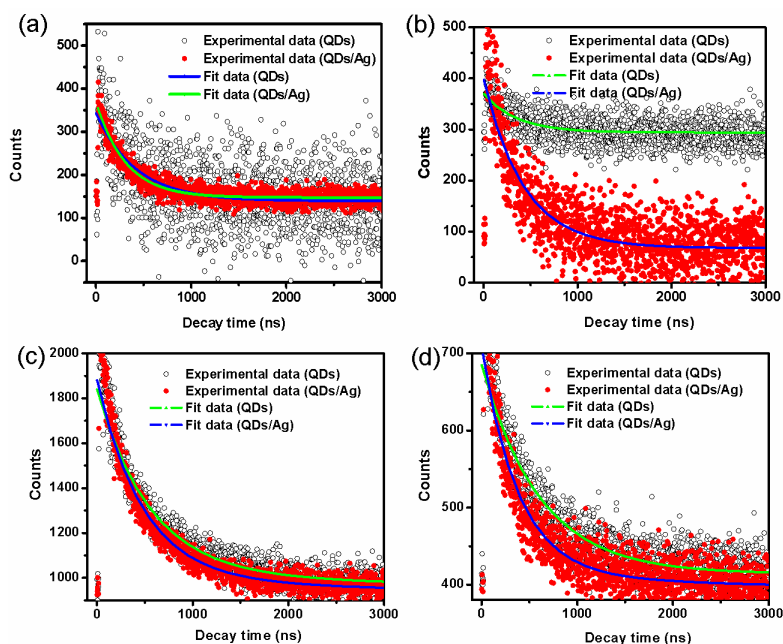


Figure S3. PL decay curves for PbS/CdS QDs with and without Ag#2 measured at the emission peak of 1350 nm with 444 nm excitation (355 ± 15 ns versus 360 ± 20 ns) (a) and 636 nm excitation (300 ± 15 ns versus 360 ± 10 ns) (b), and at the emission peak of 1460 nm with 444 nm excitation (550 ± 30 ns versus 527 ± 8 ns) (c) and 636 nm excitation (462 ± 25 ns versus 529 ± 6 ns) (d).

CHAPTER 4 CONCLUSIONS AND PERSPECTIVES

4.1 Conclusions

Silver nanocrystals have been investigated widely due to the possibility of systematically controlling their size and shape in synthesis and thereby their LSPRs. The unique physical and chemical features of Ag nanostructures lead to their wide application in many fields, such as surface enhanced spectroscopy for sensors, catalysis and biological labeling. The results of this thesis project are divided into two parts based on the synthesis and potential applications of Ag nanostructures. The study of both parts is constructive for understanding the growth mechanism, optical properties and potential applications of silver nanostructures.

Part I is mainly focused on synthesis and characterization of the 1D silver nanostructures. Two kinds of 1D silver nanostructures, silver nanorice structures and nanocarrot structures, were obtained from a facile polyol method, in which PEG 600 worked as a solvent and reducing agent, and PVP K30 acted as capping agent. The main difference between these two syntheses consists in the precursors: AgNO_3 for synthesizing silver nanorice structures and CF_3COOAg for nanocarrot structures. The crystal structures were characterized by TEM and the optical properties were characterized by extinction and EELS spectroscopy. The effects of the change of environmental refractive index on the shift of SPR peak location were also studied.

Part I is divided into two sections, each corresponding to one type of nanostructure. In Section I, we focused on studying the growth mechanism of silver nanorice structures and optimizing the experimental conditions. By modifying the synthesis, silver nanorice structures could be obtained on a large scale in high yield and their formation process was investigated. It was found that the seed selection process, based on the oxidative etching of the twinned crystals, was an indispensable step for the growth of the nanorice structures and oxygen played a critical role in this seed selection process. The major shape development stage of the nanorice structures was dominated by the oriented attachment along the $\langle 111 \rangle$ direction, directed by the non-uniform capping of PVP on different facets. The Ostwald ripening was responsible for the seed growth into the primary NPs and the lateral growth of the nanorice structures, albeit it was not straightforwardly apparent in the early stage of the anisotropic growth of the nanorice structures.

Slightly increasing temperature showed the acceleration effect on the 1D growth along the $\langle 111 \rangle$ direction, while further increase in temperature led to the disappearance of the 1D shape and induced the formation of highly faceted, two-dimensional, truncated triangular and hexagonal plates mainly bound by low energy faces of $\{111\}$. The growth mechanism of these two-dimensional plates was remarkably different from that of the nanorice structures. Instead of the oriented attachment, their growth was controlled by diffusion and dictated by the twin plane. The longitudinal SPR of the nanorice structures synthesized herein was highly sensitive to the surrounding dielectric medium, with the refractive index sensitivity as high as 820 nm RIU^{-1} , which makes it highly promising for sensor applications. Furthermore, in addition to the longitudinal resonance, the multipolar resonances in individual nanorice structures were mapped in real space by using the high-resolution EELS technique.

In Section II, we focused on the synthesis of asymmetric silver nanocarrots and corresponding characterization of their crystal structures and optical properties. Asymmetric 1D silver nanocarrot structures were synthesized in high yield for the first time. Structure characterization showed that the FCC dominated, crystalline silver nanocarrot structures feature mixed twins and stacking faults along the $\langle 111 \rangle$ longitudinal direction. The crystal structure of the silver nanocarrots was the same as that of silver nanorice structures. The SPR characteristics of the nanocarrot structures were revealed by far-field UV-Vis-NIR optical extinction spectroscopy on particle ensembles and by nanoscale EELS on individual nanocarrots. The results from both techniques were further supported by theoretical calculations. Multipolar plasmon resonances, observed by EELS, showed an interesting asymmetric distribution over the length of the nanocarrot, in contrast to the symmetric distribution observed in the nanorice structures. The longitudinal SPR peaks were red shifted and amplified in optical spectra with increasing nanocarrot length. Silver nanocarrot structures also showed high refractive index sensitivity of $890 \pm 87 \text{ nm RIU}^{-1}$, making them very attractive for sensor applications. In addition, these nanocarrot structures are also promising for, but not limited to, biological sample studies due to their tunable SPR in the NIR spectral range and optical waveguiding below the diffraction limit.

Part II focused on the surface enhanced spectroscopy investigations based on silver nanostructures, which is divided into two sections, one corresponding to SERS and the other SEF. In Section III, we focused on investigating the SERS of flower-like silver mesoparticle dimers. The dimers were performed by means of the micro-manipulation. The measured SERS

enhancements were found to be 10~100 times higher on dimers than that on individual mesoparticles. The observation of a high dependence of incident polarization illustrates that, even though the surface roughness is dominant for SERS on the individual mesoparticles with rough surface topography, the coupling effect still gives a significant additional SERS enhancement in their dimers. In addition, the use of the micro-manipulation allowed us to achieve dimers with high SERS enhancement controllably and reproducibly. This work contributed to the understanding the SERS enhancement mechanism in the roughened mesoparticles dimer system, as well as to controllably realizing SERS substrates with large “hot spot” area for high enhancement.

In section IV, we focused on the PL enhancement of plasmon/fluorophore system consisting of lead chalcogenide QDs and Ag NP film. The Ag NP/QD films have been fabricated by a layer-by-layer approach. The films exhibited a significant PL enhancement, dominated by the excitation enhancement mechanism if the spectra of the Ag NPs were not matched with emission wavelengths of QDs or if the excitation wavelength was far away from the SPR peak in the NIR range. In contrast, both the excitation and emission enhancement mechanisms could contribute to the PL enhancement once the absorption/emission spectra of QDs were matched with the resonance wavelengths of Ag NPs. Moreover, by optimizing the Ag NP/QD system, we were able to reach a PL EF as high as 2.8, due to the strong coupling between the QDs and Ag NPs. Therefore, this Ag NP/QD film holds great promises for the emerging QDs devices for the potential applications such as highly efficient light-emitting diodes, and biological sensors.

4.2 Perspectives

Facile polyol approaches were developed for synthesizing silver nanorice and nanocarrot structures for the first time. The growth was initiated by an indispensable seed-selection process through oxidatively etching twinned silver crystals and then dominated by oriented attachment and Ostwald ripening. The oriented attachment growth is believed to be dictated by the capping effect of PVP. Through this way, the major shape was decided by anisotropic growth. Through modifying reaction parameters, and/or changing capping agents or precursors, other shapes of silver nanostructures can be expected through this gentle polyol method. Moreover, this

synthesis method could be potentially extended to synthesizing other metallic materials, such as Au, Cu and Pt, with anisotropic structures.

The SPR characteristics of the nanorice and nanocarrot structures, which were revealed by far-field UV-Vis-NIR optical extinction spectroscopy on particle ensembles and by nanoscale EELS on individual structures, are interesting. For both types of nanostructures, multipolar plasmon resonances could be observed and the dipole longitudinal modes felled in the NIR range, which have potential for NIR-related applications. For example, optical detection in NIR range possesses higher potential in bio-applications due to the deeper penetration of lights and the decrease of light scattering.[53] For surface enhanced spectroscopy, if the absorption, excitation and signal are situated in the SPR ranges, the resonance will lead to the maximum enhancement. These two structures with a transverse mode in the Vis range and longitudinal mode in the NIR range could thus be used for surface enhanced spectroscopy in the NIR range, especially for bio-sensor application. Furthermore, through tuning the aspect ratio, the SPR peak position in these 1D nanostructures could be tuned to a desired range, which is another great advantage for practical applications. In addition, these two structures have sharp tips, which are expected to generate very high local EM field. For the above reasons, nanorice and nanocarrot structures could be good candidates for surface enhanced spectroscopy in the NIR range in future.

Although individual nanostructures can already generate high EM field by themselves, dimer structures can in principle provide even stronger EM enhancement than simply adding the contribution of two nanostructures together, as we mentioned in Part III. It is because that the coupling effect in the dimer could give a significant additional enhancement, and also modify the optical properties. To obtain the highest enhancement, it is important to realize the formation of dimers in a controlled fashion. In previous studies, we have successfully assembled the dimers of flower-like silver mesoparticles by means of the micro-manipulation. However, for silver nanorice or nanocarrot structures, this method is not feasible due to their smaller sizes below the manipulation limit. Molecular interactions are reported to be used in assembling nanostructures by selectively functionalizing certain facets. Because nanostructure surface is composed of a variety of crystal facets, the binding of molecules with different facets can be distinct. After functionalization with specific molecules, the binding will be preferential on specific facets. By this way, the functionalized nanostructures could be controllably assembled in solution through the interaction between molecules.

Nanorice and nanocarrot structures are novel 1D structures, if we could assemble them into dimers end-to-end or side-to-side, the effect of plasmonic coupling can be investigated and then applied into various applications. Our synthesized 1D silver nanostructures are stabilized by PVP, which prevents them from self-assembling. Some aggregations observed by SEM or TEM were considered to be the contribution of capillary forces during the sample preparation process. One way to form their dimers, in particular end-to-end dimers, may be to functionalize two ends with interacting molecules. The main difficulty is how to modify both ends of the 1D nanostructures with specific molecules while leave the side surfaces free. It is known that PVP preferentially binds to {100} facets of Ag.[6] In our 1D nanostructures, the {100} facets are the longitudinal side surfaces and {111} facets are the surface at both ends. For this reason, PVP at both ends may be more easily displaced, which allows selective functionalization and subsequent end-to-end assembling. For example, octadecanethiol, which was reported to form dimers of silver nanocubes, may be applied to help with the assembling of our 1D nanostructures.[6] To do it, octadecanethiol will be dissolved first in ethanol and then the purified nanostructures will be dispersed into this ethanol solution by sonication and incubated for certain time to functionalize them with octadecanethiol molecules. Functionalized 1D nanostructures will be thoroughly washed by repeated centrifugation-redispersion processes to remove excessive molecules before they are transferred into water for assembling. The details in experimental parameters, such as the concentration of octadecanethiol, the time of incubation, and the components of the aqueous solution will be studied to attain this goal.

REFERENCES

- [1] T.A. Wertime, *Science*, 182 (1973) 875-887.
- [2] W.A. Murray, W.L. Barnes, *Advanced Materials*, 19 (2007) 3771-3782.
- [3] T.W. Odom, *Nat. Nanotechnol.*, 7 (2012) 550-551.
- [4] S. Link, M.A. El-Sayed, *Annu. Rev. Phys. Chem.*, 54 (2003) 331-366.
- [5] I. Freestone, N. Meeks, M. Sax, C. Higgitt, *Gold Bull.*, 40 (2007) 270-277.
- [6] M. Rycenga, C.M. Cobley, J. Zeng, W.Y. Li, C.H. Moran, Q. Zhang, D. Qin, Y.N. Xia, *Chem. Rev.*, 111 (2011) 3669-3712.
- [7] K.A. Willets, R.P. Van Duyne, *Localized surface plasmon resonance spectroscopy and sensing*, in: *Annu. Rev. Phys. Chem.*, Annual Reviews, Palo Alto, 2007, pp. 267-297.
- [8] A.J. Haes, R.P. Van Duyne, *Journal of the American Chemical Society*, 124 (2002) 10596-10604.
- [9] K.M. Mayer, J.H. Hafner, *Chem. Rev.*, 111 (2011) 3828-3857.
- [10] M.E. Stewart, C.R. Anderton, L.B. Thompson, J. Maria, S.K. Gray, J.A. Rogers, R.G. Nuzzo, *Chem. Rev.*, 108 (2008) 494-521.
- [11] J.F. Li, Y.F. Huang, Y. Ding, Z.L. Yang, S.B. Li, X.S. Zhou, F.R. Fan, W. Zhang, Z.Y. Zhou, D.Y. Wu, B. Ren, Z.L. Wang, Z.Q. Tian, *Nature*, 464 (2010) 392-395.
- [12] M.C. Daniel, D. Astruc, *Chem. Rev.*, 104 (2004) 293-346.
- [13] A. Campion, P. Kambhampati, *Chem. Soc. Rev.*, 27 (1998) 241-250.
- [14] P.K. Jain, X.H. Huang, I.H. El-Sayed, M.A. El-Sayed, *Accounts of Chemical Research*, 41 (2008) 1578-1586.
- [15] L. Dykman, N. Khlebtsov, *Chem. Soc. Rev.*, 41 (2012) 2256-2282.
- [16] J. Chen, B.J. Wiley, Y. Xia, *Langmuir*, 23 (2007) 4120-4129.
- [17] R. Kolesov, B. Grotz, G. Balasubramanian, R.J. Stohr, A.A.L. Nicolet, P.R. Hemmer, F. Jelezko, J. Wrachtrup, *Nat. Phys.*, 5 (2009) 470-474.
- [18] W.L. Barnes, A. Dereux, T.W. Ebbesen, *Nature*, 424 (2003) 824-830.
- [19] C.B. Murray, C.R. Kagan, M.G. Bawendi, *Annu. Rev. Mater. Sci.*, 30 (2000) 545-610.
- [20] A.R. Tao, S. Habas, P.D. Yang, *Small*, 4 (2008) 310-325.
- [21] Y.G. Sun, Y.N. Xia, *Science*, 298 (2002) 2176-2179.
- [22] Y.N. Xia, Y.J. Xiong, B. Lim, S.E. Skrabalak, *Angew. Chem.-Int. Edit.*, 48 (2009) 60-103.
- [23] B. Wiley, Y.G. Sun, B. Mayers, Y.N. Xia, *Chemistry-a European Journal*, 11 (2005) 454-463.
- [24] S.A. Maier, H.A. Atwater, *J. Appl. Phys.*, 98 (2005).
- [25] P. Mulvaney, *Langmuir*, 12 (1996) 788-800.
- [26] V. Giannini, A.I. Fernandez-Dominguez, Y. Sonnefraud, T. Roschuk, R. Fernandez-Garcia, S.A. Maier, *Small*, 6 (2010) 2498-2507.
- [27] J. Dorfmüller, R. Vogelgesang, R.T. Weitz, C. Rockstuhl, C. Etrich, T. Pertsch, F. Lederer, K. Kern, *Nano Letters*, 9 (2009) 2372-2377.
- [28] Y. Fang, H. Wei, F. Hao, P. Nordlander, H. Xu, *Nano Letters*, 9 (2009) 2049-2053.
- [29] E. Hutter, J.H. Fendler, *Advanced Materials*, 16 (2004) 1685-1706.
- [30] A.M. Schwartzberg, J.Z. Zhang, *Journal of Physical Chemistry C*, 112 (2008) 10323-10337.
- [31] S. Link, M.A. El-Sayed, *J. Phys. Chem. B*, 103 (1999) 8410-8426.
- [32] Z.P. Li, H.X. Xu, *J. Quant. Spectrosc. Radiat. Transf.*, 103 (2007) 394-401.
- [33] B.J. Wiley, S.H. Im, Z.Y. Li, J. McLellan, A. Siekkinen, Y.N. Xia, *J. Phys. Chem. B*, 110 (2006) 15666-15675.
- [34] B.S. Guiton, V. Iberi, S. Li, D.N. Leonard, C.M. Parish, P.G. Kotula, M. Varela, G.C. Schatz, S.J. Pennycook, J.P. Camden, *Nano Letters*, 11 (2011) 3482-3488.
- [35] H. Wei, A. Reyes-Coronado, P. Nordlander, J. Aizpurua, H. Xu, *Acs Nano*, 4 (2010) 2649-2654.

- [36] J. Dorfmueller, R. Vogelgesang, W. Khunsin, C. Rockstuhl, C. Etrich, K. Kern, *Nano Letters*, 10 (2010) 3596-3603.
- [37] D. Rossouw, G.A. Botton, *Optics Express*, 20 (2012) 6968-6973.
- [38] P.K. Jain, K.S. Lee, I.H. El-Sayed, M.A. El-Sayed, *J. Phys. Chem. B*, 110 (2006) 7238-7248.
- [39] E. Prodan, C. Radloff, N.J. Halas, P. Nordlander, *Science*, 302 (2003) 419-422.
- [40] Y. Yang, J. Shi, T. Tanaka, M. Nogami, *Langmuir*, 23 (2007) 12042-12047.
- [41] T. Ming, H.J. Chen, R.B. Jiang, Q. Li, J.F. Wang, *J. Phys. Chem. Lett.*, 3 (2012) 191-202.
- [42] H.J. Chen, L. Shao, K.C. Woo, T. Ming, H.Q. Lin, J.F. Wang, *Journal of Physical Chemistry C*, 113 (2009) 17691-17697.
- [43] J.A. Schuller, E.S. Barnard, W.S. Cai, Y.C. Jun, J.S. White, M.L. Brongersma, *Nature Materials*, 9 (2010) 193-204.
- [44] D.K. Gramotnev, S.I. Bozhevolnyi, *Nat. Photonics*, 4 (2010) 83-91.
- [45] J. Kneipp, H. Kneipp, K. Kneipp, *Chem. Soc. Rev.*, 37 (2008) 1052-1060.
- [46] N.P.W. Pieczonka, R.F. Aroca, *Chem. Soc. Rev.*, 37 (2008) 946-954.
- [47] H.X. Xu, E.J. Bjerneld, M. Kall, L. Borjesson, *Physical Review Letters*, 83 (1999) 4357-4360.
- [48] Z.Q. Tian, B. Ren, D.Y. Wu, *J. Phys. Chem. B*, 106 (2002) 9463-9483.
- [49] S.C. Glotzer, M.J. Solomon, *Nature Materials*, 6 (2007) 557-562.
- [50] A. Otto, I. Mrozek, H. Grabhorn, W. Akemann, *J. Phys.-Condes. Matter*, 4 (1992) 1143-1212.
- [51] A. Otto, *J. Raman Spectrosc.*, 36 (2005) 497-509.
- [52] H. Liang, Z. Li, W. Wang, Y. Wu, H. Xu, *Advanced Materials*, 21 (2009) 4614-4618.
- [53] X.M. Qian, X.H. Peng, D.O. Ansari, Q. Yin-Goen, G.Z. Chen, D.M. Shin, L. Yang, A.N. Young, M.D. Wang, S.M. Nie, *Nature Biotechnology*, 26 (2008) 83-90.
- [54] U. Resch-Genger, M. Grabolle, S. Cavaliere-Jaricot, R. Nitschke, T. Nann, *Nat. Methods*, 5 (2008) 763-775.
- [55] F. Terenziani, C. Katan, E. Badaeva, S. Tretiak, M. Blanchard-Desce, *Advanced Materials*, 20 (2008) 4641-4678.
- [56] A.L. Rogach, A. Eychmueller, S.G. Hickey, S.V. Kershaw, *Small*, 3 (2007) 536-557.
- [57] G. Konstantatos, I. Howard, A. Fischer, S. Hoogland, J. Clifford, E. Klem, L. Levina, E.H. Sargent, *Nature*, 442 (2006) 180-183.
- [58] B.J. Yang, N. Lu, D.P. Qi, R.P. Ma, Q. Wu, J.Y. Hao, X.M. Liu, Y. Mu, V. Reboud, N. Kehagias, C.M.S. Torres, F.Y.C. Boey, X.D. Chen, L.F. Chi, *Small*, 6 (2010) 1038-1043.
- [59] J.R. Lakowicz, *Anal. Biochem.*, 337 (2005) 171-194.
- [60] K. Aslan, I. Gryczynski, J. Malicka, E. Matveeva, J.R. Lakowicz, C.D. Geddes, *Curr. Opin. Biotechnol.*, 16 (2005) 55-62.
- [61] J.R. Lakowicz, *Plasmonics*, 1 (2006) 5-33.
- [62] E. Fort, S. Gresillon, *J. Phys. D-Appl. Phys.*, 41 (2008).
- [63] T.K. Sau, A.L. Rogach, F. Jackel, T.A. Klar, J. Feldmann, *Advanced Materials*, 22 (2010) 1805-1825.
- [64] O. Hess, J.B. Pendry, S.A. Maier, R.F. Oulton, J.M. Hamm, K.L. Tsakmakidis, *Nature Materials*, 11 (2012) 573-584.
- [65] D.R. Jung, J. Kim, S. Nam, C. Nahm, H. Choi, J.I. Kim, J. Lee, C. Kim, B. Park, *Appl. Phys. Lett.*, 99 (2011) 041906.
- [66] P.P. Pompa, L. Martiradonna, A. Della Torre, F. Della Sala, L. Manna, M. De Vittorio, F. Calabi, R. Cingolani, R. Rinaldi, *Nat. Nanotechnol.*, 1 (2006) 126-130.
- [67] K. Tanaka, E. Plum, J.Y. Ou, T. Uchino, N.I. Zheludev, *Physical Review Letters*, 105 (2010) 227403.
- [68] Y. Jiang, H.-Y. Wang, H. Wang, B.-R. Gao, Y.-w. Hao, Y. Jin, Q.-D. Chen, H.-B. Sun, *The Journal of Physical Chemistry C*, 115 (2011) 12636-12642.
- [69] H. Naiki, S. Masuo, S. Machida, A. Itaya, *The Journal of Physical Chemistry C*, 115 (2011) 23299-23304.

- [70] Y.C. Chen, K. Munechika, I. Jen-La Plante, A.M. Munro, S.E. Skrabalak, Y.N. Xia, D.S. Ginger, *Appl. Phys. Lett.*, 93 (2008) 053106.
- [71] X. Ma, H. Tan, T. Kipp, A. Mews, *Nano Letters*, 10 (2010) 4166-4174.
- [72] K. Munechika, Y. Chen, A.F. Tillack, A.P. Kulkarni, I.J.L. Plante, A.M. Munro, D.S. Ginger, *Nano Letters*, 10 (2010) 2598-2603.
- [73] K. Munechika, Y.C. Chen, A.F. Tillack, A.P. Kulkarni, I. Jen-La Plante, A.M. Munro, D.S. Ginger, *Nano Letters*, 11 (2011) 2725-2730.
- [74] A.I. Dragan, E.S. Bishop, J.R. Casas-Finet, R.J. Strouse, J. McGivney, M.A. Schenerman, C.D. Geddes, *Plasmonics*, 7 (2012) 739-744.
- [75] T. Ozel, S. Nizamoglu, M.A. Sefunc, O. Samarskaya, I.O. Ozel, E. Mutlugun, V. Lesnyak, N. Gaponik, A. Eychemuller, S.V. Gaponenko, H.V. Demir, *Acs Nano*, 5 (2011) 1328-1334.
- [76] X.D. Fan, I.M. White, S.I. Shopova, H.Y. Zhu, J.D. Suter, Y.Z. Sun, *Anal. Chim. Acta*, 620 (2008) 8-26.
- [77] C.J. Murphy, A.M. Gole, S.E. Hunyadi, J.W. Stone, P.N. Sisco, A. Alkilany, B.E. Kinard, P. Hankins, *Chemical Communications*, (2008) 544-557.
- [78] S. Lal, S. Link, N.J. Halas, *Nat. Photonics*, 1 (2007) 641-648.
- [79] R. Gordon, D. Sinton, K.L. Kavanagh, A.G. Brolo, *Accounts of Chemical Research*, 41 (2008) 1049-1057.
- [80] H. Liang, H. Zhao, D. Rossouw, W. Wang, H. Xu, G.A. Botton, D. Ma, *Chemistry of Materials*, 24 (2012) 2339-2346.
- [81] F. Lopez-Tejiera, R. Paniagua-Dominguez, J.A. Sanchez-Gil, *Acs Nano*, 6 (2012) 8989-8996.
- [82] D.D. Evanoff, G. Chumanov, *ChemPhysChem*, 6 (2005) 1221-1231.
- [83] J.H. Wang, T.H. Yang, W.W. Wu, L.J. Chen, C.H. Chen, C.J. Chu, *Nanotechnology*, 17 (2006) 719-722.
- [84] A. Jakab, C. Rosman, Y. Khalavka, J. Becker, A. Truegler, U. Hohenester, C. Soennichsen, *Acs Nano*, 5 (2011) 6880-6885.
- [85] D.H. Son, S.M. Hughes, Y.D. Yin, A.P. Alivisatos, *Science*, 306 (2004) 1009-1012.
- [86] Y. Tang, M. Ouyang, *Nature Materials*, 6 (2007) 754-759.
- [87] S.H. Im, Y.T. Lee, B. Wiley, Y.N. Xia, *Angew. Chem.-Int. Edit.*, 44 (2005) 2154-2157.
- [88] Y. Wang, Y.Q. Zheng, C.Z. Huang, Y.N. Xia, *Journal of the American Chemical Society*, 135 (2013) 1941-1951.
- [89] H. Liang, W. Wang, Y. Huang, S. Zhang, H. Wei, H. Xu, *The Journal of Physical Chemistry C*, 114 (2010) 7427-7431.
- [90] M.R. Langille, J. Zhang, M.L. Personick, S.Y. Li, C.A. Mirkin, *Science*, 337 (2012) 954-957.
- [91] R.C. Jin, Y.W. Cao, C.A. Mirkin, K.L. Kelly, G.C. Schatz, J.G. Zheng, *Science*, 294 (2001) 1901-1903.
- [92] B.J. Wiley, Y. Chen, J.M. McLellan, Y. Xiong, Z.-Y. Li, D. Ginger, Y. Xia, *Nano Letters*, 7 (2007) 1032-1036.
- [93] H. Liang, H. Yang, W. Wang, J. Li, H. Xu, *Journal of the American Chemical Society*, 131 (2009) 6068-6069.
- [94] J. Zhang, M.R. Langille, C.A. Mirkin, *Nano Letters*, 11 (2011) 2495-2498.
- [95] P.C. Lee, D. Meisel, *J. Phys. Chem.*, 86 (1982) 3391-3395.
- [96] A.L. Koh, K. Bao, I. Khan, W.E. Smith, G. Kothleitner, P. Nordlander, S.A. Maier, D.W. McComb, *Acs Nano*, 3 (2009) 3015-3022.
- [97] J.P. Camden, J.A. Dieringer, Y.M. Wang, D.J. Masiello, L.D. Marks, G.C. Schatz, R.P. Van Duyne, *Journal of the American Chemical Society*, 130 (2008) 12616-+.
- [98] L.T. Qu, L.M. Dai, *J. Phys. Chem. B*, 109 (2005) 13985-13990.
- [99] S.Q. Wang, H. Zhao, Y. Wang, C.M. Li, Z.H. Chen, V. Paulose, *Applied Physics B-Lasers and Optics*, 92 (2008) 49-52.
- [100] B.J. Wiley, Z.H. Wang, J. Wei, Y.D. Yin, D.H. Cobden, Y.N. Xia, *Nano Letters*, 6 (2006) 2273-2278.

- [101] X.S. Shen, G.Z. Wang, X. Hong, X. Xie, W. Zhu, D.P. Li, *Journal of the American Chemical Society*, 131 (2009) 10812-10813.
- [102] X. Huang, S. Li, S. Wu, Y. Huang, F. Boey, C.L. Gan, H. Zhang, *Advanced Materials*, 24 (2012) 979-983.
- [103] H.Y. Liang, D. Rossouw, H.G. Zhao, S.K. Cushing, H.L. Shi, A. Korinek, H.X. Xu, F. Rosei, W.Z. Wang, N.Q. Wu, G.A. Botton, D.L. Ma, *Journal of the American Chemical Society*, 135 (2013) 9616-9619.
- [104] D.-K. Lim, K.-S. Jeon, H.M. Kim, J.-M. Nam, Y.D. Suh, *Nature Materials*, 9 (2010) 60-67.
- [105] H.Y. Liang, Z.P. Li, Z.X. Wang, W.Z. Wang, F. Rosei, D.L. Ma, H.X. Xu, *Small*, 8 (2012) 3400-3405.
- [106] E.J.D. Klem, D.D. MacNeil, L. Levina, E.H. Sargent, *Advanced Materials*, 20 (2008) 3433-3439.
- [107] Q.-A. Zhang, W.-Y. Li, L.P. Wen, J.Y. Chen, Y.N. Xia, *Chemistry-a European Journal*, 16 (2010) 10234-10239.
- [108] H. Zhao, M. Chaker, D. Ma, *Journal of Physical Chemistry C*, 113 (2009) 6497-6504.
- [109] F.J. Garcia de Abajo, *Reviews of Modern Physics*, 82 (2010) 209-275.
- [110] D.C. Joy, C.S. Joy, *Micron*, 27 (1996) 247-263.
- [111] G.L. Hornyak, S. Peschel, T. Sawitowski, G. Schmid, *Micron*, 29 (1998) 183-190.
- [112] G.W.C. Silva, L.Z. Ma, O. Hemmers, D. Lindle, *Micron*, 39 (2008) 269-274.
- [113] J.I. Langford, D. Louer, *Rep. Prog. Phys.*, 59 (1996) 131-234.
- [114] K.D.M. Harris, M. Tremayne, B.M. Kariuki, *Angew. Chem.-Int. Edit.*, 40 (2001) 1626-1651.
- [115] O. Nicoletti, M. Wubs, N.A. Mortensen, W. Sigle, P.A. van Aken, P.A. Midgley, *Optics Express*, 19 (2011) 15371-15379.
- [116] D. Rossouw, M. Couillard, J. Vickery, E. Kumacheva, G.A. Botton, *Nano Letters*, 11 (2011) 1499-1504.
- [117] M.-W. Chu, V. Myroshnychenko, C.H. Chen, J.-P. Deng, C.-Y. Mou, F. Javier Garcia de Abajo, *Nano Letters*, 9 (2009) 399-404.
- [118] T.R. Jensen, G.C. Schatz, R.P. Van Duyne, *J. Phys. Chem. B*, 103 (1999) 2394-2401.
- [119] P.B. Johnson, R.W. Christy, *Physical Review B*, 6 (1972) 4370-4379.

RÉSUMÉ

L'introduction

Dans l'histoire de l'humanité, trois éléments non-radioactifs du groupe 11 du tableau périodique : le cuivre, l'argent et l'or ont joué un rôle important depuis l'utilisation de la monnaie.[1] Les pièces de monnaie métalliques ont une apparence brillante grâce à leur excellente propriété réfléchissante de la lumière visible (Vis) et des couleurs intenses par couplage à la lumière.[2] Leur performance optique fascinante appelée résonance plasmonique de surface (RPS) a beaucoup d'applications. Par exemple, les artisans exploitent les nanostructures des pièces de monnaie métalliques comme colorants dans les toiles, les vitraux colorés et les céramiques.[3, 4] Aujourd'hui, la recherche en RPS a suscité beaucoup d'intérêts grâce à sa capacité de manipuler efficacement la lumière à une échelle très petite par rapport la longueur d'onde et ses applications potentielles, qui va bien au-delà des espérances.

Un plasmon dans un métal est l'oscillation collective et quantifiée des électrons de conduction, excités par un rayonnement électromagnétique (EM).[18, 24, 25] D'un point de vue classique, les électrons libres mobiles se repoussent entre eux et sont attirés par les noyaux d'ions positifs fixes dans un métal. Sous un champ EM extérieur variant dans le temps, les électrons seront forcés à osciller collectivement contre la force de rappel des noyaux positifs jusqu'à ce que l'énergie soit perdue par résistance ou amortissement. Une quantification de ce type d'oscillation est le plasmon. Il existe deux types de modes plasmoniques : (i) les plasmons de surface localisés non-propagatifs (PSL) et (ii) les plasmons de surface propagatifs.[2, 6] Les PSL sont soutenus par des nanostructures de taille inférieure ou comparable à la longueur d'onde d'excitation en trois dimensions. Les PSL peuvent être excités lorsque la fréquence d'excitation est égale à leur fréquence naturelle, et une forte résonance se produit, communément connu comme résonance des plasmons de surface localisés (RPSL). La RPSL mène à une forte dispersion de la lumière, une forte absorption et une amplification maximale du champ EM local.[9] Les caractéristiques des RPSL dépendent de la composition, de la taille et de la forme des nanostructures et leur milieu diélectrique. Par exemple, lorsque la taille des particules augmente, l'absorption et la dispersion augmentent également.[17] Dans le même temps, la position du pic de RPSL sera décalé vers le rouge et la largeur sera élargie. La forme est un autre paramètre critique pour les caractéristiques des RPSL.[33] Par exemple, les nanostructures sphériques ne montrent qu'un pic

de RPSL en général, mais les nanostructures unidimensionnelles (1D) soutiennent les résonances transversales et longitudinales. Ces dernières sont ajustées par contrôle du rapport d'aspect et/ou la longueur.[15, 34] En outre, avec une augmentation du rapport d'aspect, des modes de RPSL multipolaires d'ordre plus élevé peuvent être excités.[27, 35-37]

Le domaine de la recherche sur les plasmons s'appelle "plasmonique". Il se focalise sur les interactions métal-lumière qui sont liées à la localisation, la direction et la manipulation des ondes EM au-delà de la limite de diffraction et jusqu'à l'échelle nanométrique.[6, 18, 24, 26] Dans ce domaine de recherche, les nanostructures métalliques sont utilisées comme des antennes pour convertir la lumière en champ EM localisé comme des capteurs pour détecter une variation dans le milieu diélectrique local, et comme guide-d'ondes pour confiner et acheminer la lumière sous de la limite de diffraction classique. Ces propriétés peuvent conduire à de nombreuses applications, comme les capteurs chimiques et biochimiques,[8-10] la thérapie photothermique[12, 14, 15] et les guide-d'ondes nanophotoniques.[16-18] Toutes ces applications dépendent fortement des interactions métal-lumière. Un contrôle précis de la taille, la forme, et/ou l'espacement des nanostructures, la lumière peut être contrôlée et manipulée de façon efficace avec une précision sans précédent.[14] Le développement de nouvelles méthodes permet de réaliser ce niveau de contrôle.[19-22] Ces instruments de contrôle exceptionnel et de détection avancé, en combinaison avec de puissants outils de modélisation EM ont fourni une meilleure compréhension des interactions métal-lumière.[10] Parmi les métaux, l'argent a suscité plus d'intérêt dans la recherche plasmonique, et ses propriétés avantageuses ont conduit à la plupart des applications dans des domaines pertinents.[6, 21, 23]

Une attention particulière a été portée sur les nanostructures d'argent grâce à leurs propriétés physiques et chimiques uniques dont le matériau volumineux ne possède pas. Le contrôle de la taille et de la forme des nanostructures d'Ag pour définir leur caractéristique plasmonique unique est important pour des raisons pratiques. En général, les nanostructures d'Ag peuvent être synthétisées à partir de deux méthodes principales, une méthode chimique et une méthode physique. La méthode chimique est la plus répandue. Elle consiste à produire des atomes d'Ag à partir de précurseurs par réduction et par conséquent leur croissance en nanostructures à l'aide d'un agent stabilisant. Des nanostructures d'argent de différentes morphologies bien contrôlées, telles que sphère,[23, 89] cube,[87] icosaèdre,[90] nanoprisme triangulaire,[91] barre,[92] riz,[92, 93] tige[94] et fil[16] peuvent être synthétisées par méthode chimique. Les caractéristiques

plasmoniques dépendant de la taille et la forme de nanostructures d'argent ont mené à de larges applications dans de nombreux domaines, comme la spectroscopie de surface augmentée la catalyse et identifications biologique. Attiré par des applications potentielles, le travail effectué dans cette thèse est centré sur la synthèse et les propriétés des nanostructures d'argent.

Objectif de la thèse

Partie I: Synthèse

Même si certaines nanostructures d'Ag ont été synthétisées par des méthodes ci-dessus, c'est difficile de synthétiser des structures de nanoriz d'argent uniformes avec une reproductibilité élevée. Le mécanisme de croissance de ces nanostructures n'est pas bien compris et les connaissances sur la forme déterminant des paramètres sont également limitées. La compréhension de ces aspects peut potentiellement conduire à un meilleur contrôle de la reproductibilité, l'uniformité de la forme, et le rendement de la forme synthétisée de ces structures du nanoriz. En outre, leurs propriétés optiques ont besoin d'une investigation plus approfondie avant leurs applications pratiques. En outre, même si certaines nanostructures 1D d'Ag ont été obtenues à partir de solution, principalement elles sont fortement symétriques. Cette caractéristique est attribuée à la symétrie cristalline à structure cubique à faces centrées (CFC), qui inhibe la croissance asymétrique.[22] Les exemples de nanostructures asymétriques de 1D ont été très rarement rapportés, comme des nanobattes du Cu,[83] des tiges d'aiguille et des hélico-nanostructures d'argent de ceinture plat[101] et des nanofils d'or en forme de têtard. [102] Cependant, une analyse détaillée des propriétés plasmiques de ces nanostructures asymétriques est demandée. La préparation contrôlée de nanostructures d'argent asymétriques avec des pics RPS utilisant une simple méthode de synthèse de la solution est donc souhaitable dans la création de nouvelles plates-formes pour explorer la morphologie dépendant de propriétés optiques, mais restant un défi important.

Compte tenu des écarts dans la synthèse et la compréhension, dans la partie I, nous avons étudié le processus de croissance des structures de nanoriz et nanocarottes d'argent. Les propriétés optiques de ces structures d'argent ont été étudiées plus profondément. Les objectifs de la partie I sont:

1. L'étude du mécanisme de croissance des structures de nanoriz d'argent. En comprenant le mécanisme de croissance, on peut avoir une meilleure optimisation et gagner plus de contrôle sur

la synthèse pour atteindre des nanostructures d'argent réglables en modifiant les paramètres de la réaction.

2. Synthétiser des nouvelles structures asymétriques de nanocarotte d'argent et étudier leur rapport de structure/propriété. En même temps, le mécanisme de croissance a été simplement étudié.
3. Analyser les propriétés plasmiqes des deux structures en détail par spectroscopie d'extinction optique et spectroscopie de perte d'énergie des électrons (SPEE).
4. Mesure de la sensibilité des deux structures vis-à-vis l'indice de réfraction de leurs environnements.

Partie II: Application potentielle

La spectroscopie de surface augmentée, comme la dispersion Raman de surface renforcée (DRSR) et la fluorescence de surface renforcée (FSR) est une des applications populaires de nanostructures plasmiqes d'argent. Pour ces applications, les substrats et les longueurs d'onde d'excitation sont des facteurs essentiels qui influent sur le renforcement observé. Des rayonnements de proche infrarouge (PIR) et visibles sont généralement utilisés pour exciter les modes RPS à fournir un renforcement maximal. Pour les substrats métalliques, la distribution d'intensité de champ EM est non uniforme et dépend fortement de leur morphologie. Des nanostructures avec les courbures de surface aiguë [52] et les jonctions [104] peuvent produire de grands renforcements EM. De plus, pour réaliser le couplage fort entre les plasmons de nanostructures adjacentes, une distance inférieure à quelques nanomètres est souhaitée, mais elle est difficile à contrôler. Ces écarts ou des jonctions s'appuient sur l'assemblage aléatoire de petites particules. Bien que beaucoup de recherches ont mis l'accent sur les applications basées sur le concept de la spectroscopie de surface augmentée, la production fiable, reproductible et des substrats très sensible pour les applications de détection a été un grand défi.

Des particules d'argent individuelles en forme de fleur avec une surface rugueuse ont donné d'excellentes performances dans DRSR.[52] Des dimères de facteurs de renforcement (FR) étaient 10-100 fois plus grands que celle des particules individuelles, qui ont été confirmées par mes expériences. Ces augmentations de DRSR pourraient provenir le renforcement du champ supplémentaire dans les écarts interparticulaires. L'étude du mécanisme de renforcements et de la manipulation de la formation de dimères est nécessaire pour les applications de DRSR.

RSF de points quantiques colloïdaux (PQ) a suscité beaucoup d'intérêt. Parmi tous les types de PQ, des PQ de chalcogénures de plomb ont un grand rayon de Bohr d'excitation et les petites bandes interdites en masse en permettant ainsi de confinement quantique dans très grandes tailles relatives de PQ avec une accordable émission IR.[56, 57, 106] Le comportement complexe de l'interaction plasmique/fluorophore a besoin de recherches pour comprendre et contrôler des contributions relatives du renforcement d'absorption de lumière et des modifications des taux de décroissance radiatifs et non radiative, tout cela étant crucial pour l'avancement des études théoriques et des applications pratiques.

Par conséquent, les objectifs de la partie II sont:

1. Investigation du DRSR incident qui dépend de la polarisation de dimères de particules d'argent en forme de fleur et la manipulation de particules individuelles pour former ou rompre des dimères afin d'étudier le mécanisme de renforcement *in situ*.
2. Système de fabrication couplé plasmique/fluorophore comprend des PQ de chalcogénures de plomb et des films de nanoparticules (NP) d'Ag et l'étude de l'amélioration.

Dans la partie I, deux types de nanostructures d'argent unidimensionnelles (1D), spécifiquement des structures de nanoriz et des structures de nanocarotte ont été synthétisés par une simple méthode de polyol. Le polyéthylène glycol 600 a été utilisé comme solvant et agent réducteur, et la polyvinylpyrrolidone (PVP) a agi comme élément de recouvrement. Le principal facteur menant aux différentes morphologies des produits, est le fait que le précurseur de AgNO_3 a été utilisé pour la synthèse de structures nanoriz d'argent tandis que CF_3COOAg pour les structures de nanocarotte. Les détails de la structure ont été caractérisés par microscopie électronique à transmission (MET) et la diffraction des rayons X (DRX). Les propriétés optiques ont été caractérisés par des spectres d'extinction optique UV -Vis -PIR et SPEE. Dans le détail, la partie I est divisée en deux sections basées sur deux types de nanostructures.

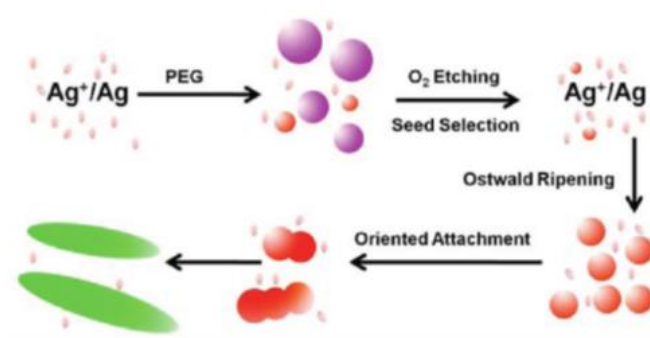


Figure R1. Processus de croissance proposé des structures de nanoriz d'argent (rouge: monocristal; violet: cristal jumelé et rose: Ag⁰ ou Ag⁺, vert: nanoriz).

Dans la section I, l'investigation a été concentrée sur l'étude du mécanisme de croissance des structures de nanoriz d'argent et l'optimisation des conditions expérimentales. En modifiant les paramètres de synthèse, des structures nanoriz d'Ag pourraient être obtenus sur un haut rendement à une grande échelle. Leur processus de croissance a été manipulé pour comprendre leur mécanisme de croissance. Les résultats ont montré que le processus de sélection des semences, basé sur l'attaque oxydative des cristaux jumelés, est une étape indispensable et l'oxygène joue un rôle critique dans ce processus de sélection des semences. (Figure R1) Le stade de développement de la forme majeure des structures de nanoriz est dominé par l'attachement orienté selon la direction $\langle 111 \rangle$, réalisé par l'écrêtement non uniforme de la PVP sur différentes facettes. (Figure R2) La maturation d'Ostwald est responsable pour la croissance de la semence dans les nanostructures primaires et la croissance latérale des structures de nanoriz mais il n'est pas clairement évident dans le stade précoce de la croissance anisotrope de structures de nanoriz. La température légèrement croissante montre l'accélération de la croissance, tandis que l'augmentation de la température se conduit à la disparition de la forme 1D et induit la formation de triangulaires tronqués, bidimensionnelles, multi-facettes et des plaques hexagonales liés principalement par des faces de faible énergie de $\{111\}$. Le mécanisme de la croissance de ces plaques à deux dimensions est très différent que celle des structures de nanoriz. Au lieu de l'attachement orienté, leur croissance est contrôlée par la diffusion et dicté par le plan de macle. La RPS longitudinale des structures de nanoriz synthésés est très sensible à l'environnement du milieu diélectrique, avec la sensibilité de l'indice de réfraction plus élevé que 820 nm RIU^{-1} (RIU, par unité d'indice de réfraction), ce qui est très prometteur pour les

applications de capteurs. En outre, les résonances multipolaires dans la structure de nanoriz individuelle ont été cartographiées dans l'espace réel en utilisant la technique de SPEE.

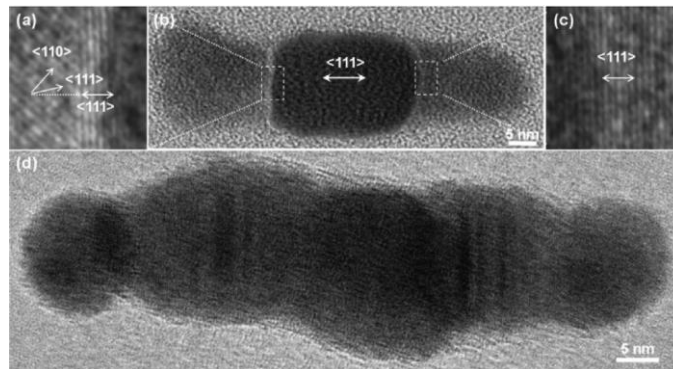


Figure R2. Attachement orienté des PQ d'argent. Les panneaux (a) et (c) sont des images de MET avec haute résolution de la zone sélectionnée mise en évidence par les rectangles en (b).

Les résultats correspondants de cette section sont présentés dans la publication[80]:

[80] H. Liang, H. Zhao, D. Rossouw, W. Wang, H. Xu, G.A. Botton, D. Ma, Chemistry of Materials, 24 (2012) 2339-2346.

Dans la section II, nous nous sommes concentrés sur la synthèse des structures de nanocarotte d'Ag asymétriques et la caractérisation correspondante. Des structures de nanocarotte d'argent 1D asymétriques ont été synthétisées avec un rendement élevé pour la première fois. (Figure R3) La caractérisation structurale montre que le CFC domine, le comportement de structures cristallines de nanocarotte d'argent mélange des défauts d'empilement et jumeaux sur la direction longitudinale $\langle 111 \rangle$. La structure cristalline de nanocarotte d'Ag est la même que celle des structures de nanoriz d'argent.

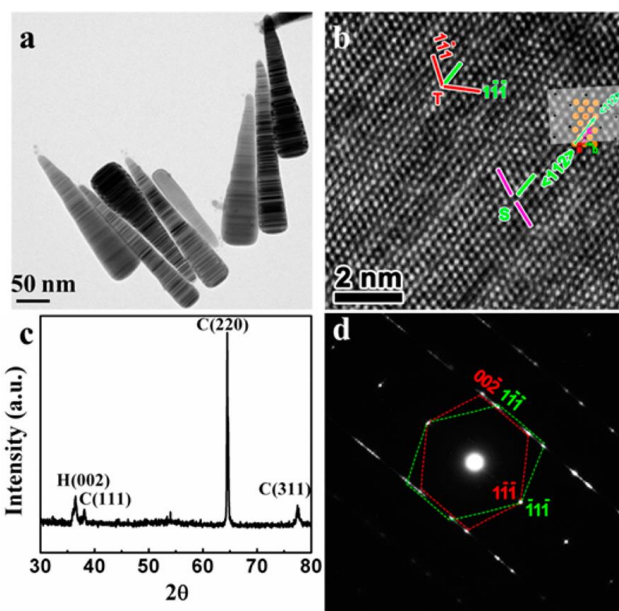


Figure R3. (a) Image MET et (c) diagramme de DRX de nanocarottes d'argent. (b) Image de MET à haute résolution, et (d) diagramme de diffraction d'électrons à la zone sélectionnée correspondante de la partie centrale d'une nanocarotte individuelle. Dans (b), les fautes d'empilement et jumeaux sont étiquetés comme T et S, respectivement.

Les caractéristiques de RPS des structures de nanocarotte ont été étudiées par spectroscopie d'extinction optique UV-VIS-PIR à des ensembles de particules et par SPEE nanométriques sur la structure de nanocarotte individuelle. Les résultats des deux techniques ont ensuite été pris en charge par des calculs théoriques. (Figure R4) Des résonances plasmiques multipolaires, observées par SPEE, montrent une distribution asymétrique intéressante sur la longueur de la structure de nanocarotte, contrairement à la distribution symétrique observée dans les structures de nanoriz. Les pics longitudinales de RPS sont décalés vers le rouge et amplifiés dans les spectres optiques avec la longueur augmentée de la structure de nanocarotte. Des structures de nanocarotte d'argent montrent également la sensibilité à l'indice de réfraction élevé de 890 ± 87 nm RIU⁻¹, ce qui est très attractif pour les applications de capteurs. En outre, ces structures de nanocarotte sont également prometteuses non seulement pour les études d'échantillons biologiques en raison de leur RPS accordable dans la gamme spectrale PIR et le guide d'onde optique en dessous de la limite de diffraction.

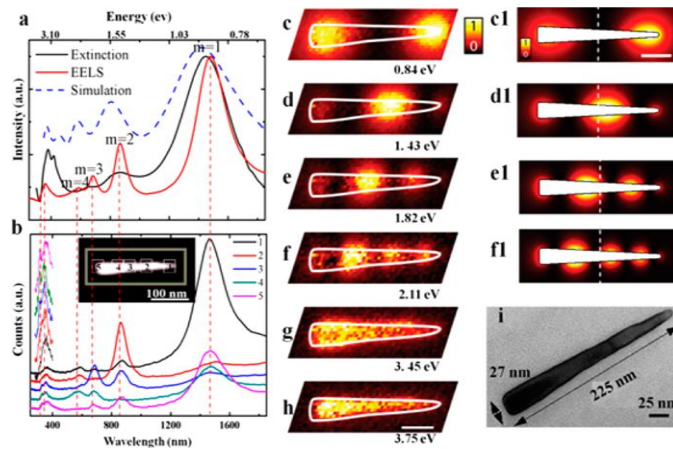


Figure R4. (a) Comparaison du spectre SPEE d'une nanocarotte montrée en (i) avec le spectre d'extinction optique expérimentale et simulé. (b) des signaux de SPEE acquis à cinq endroits différents. La zone rectangulaire définit les limites de la zone détectée par le spectre total de (a). Les spectres ont été déplacés verticalement pour clarté et les pics de RPS transversales ont été agrandis. Les pointillés rouges (a) et (b) sont des guides pour l'œil joignant les mêmes modes de résonance. (c-h) Des cartes expérimentales de résonances plasmiques multiples ont été excitées dans la nanocarotte extraite à des énergies appartenant à des pics dans le signal de SPEE. (c1-f1) des cartes calculées. Les barreaux d'échelle dans (h) et (c1) sont 50 nm. (i) image de MET de la nanocarotte choisie pour la cartographie de SPEE.

Publication des résultats présentés dans cette section sont[103]:

[103] H.Y.Liang, D. Rossouw, H.G.Zhao, S.K.Cushing, H.L.Shi, A.Korinek, H.X.Xu, F. Rosei, W.Z.Wang, N.Q. Wu, G. A.Botton, D.L.Ma. J. Am. Chem. Soc., 2013, 135, 9616.

La partie II est focalisée sur des investigations de la spectroscopie de surface renforcée basée sur des nanostructures d'argent et est également divisée en deux sections, correspondant à DRSR (Section III) et RSF (Section V), respectivement. Dans la section III, nous nous sommes concentrés sur l'étude des DRSR de dimères de particules d'argent en forme de fleur. Les dimères ont été effectués de manière contrôlée au moyen de micromanipulation. Les renforcements de DRSR sont mesurés de 10~100 fois plus élevés que celle de dimères sur mesoparticules individuelles. (Figure R5) L'observation de la forte dépendance de la DRSR sur la polarisation incidente illustre cela, même si la rugosité de surface est dominée pour DRSR sur les mesoparticules individuelles avec la topographie de surface rugueuse, l'effet de couplage donne encore un important renforcement supplémentaire de DRSR dans leurs dimères. En outre, l'utilisation de la micromanipulateur nous permet de réaliser des dimères avec un fort renforcement de DRSR contrôlé et reproductible. Ce travail contribue à la compréhension du mécanisme de renforcement de DRSR dans un système de dimère mesoparticules rugueuses,

ainsi que pour la réalisation contrôlée des substrats de DRSR avec une large “chaude” zone pour un renforcement important.

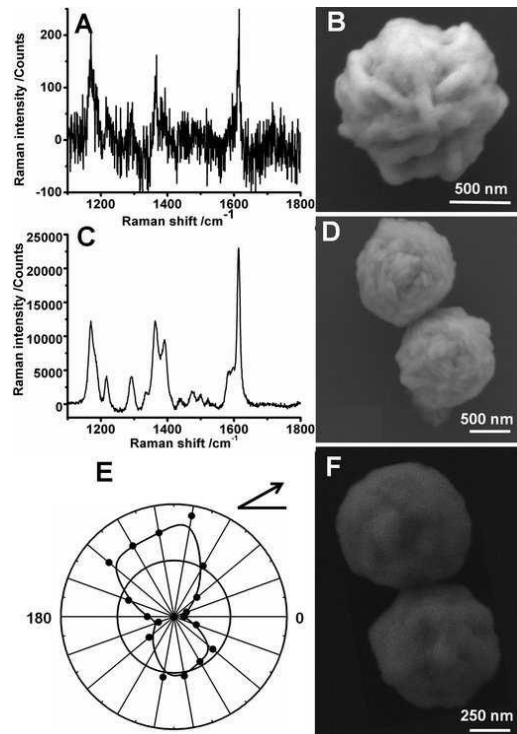


Figure R5. A) Spectre de DRSR détecté à partir d’une mesoparticule individuelle en forme de fleur et B) son image correspondante au microscope électronique à balayage (MEB). C) spectre de DRSR détecté à partir d’un dimère et D) son image de MEB correspondante. E) tracés polaires des intensités des pics Raman de 1615 cm^{-1} détectés à partir d’un dimère et F) l’image MEB correspondante, qui montre que l’angle de rotation de l’axe du dimère est d’environ 120 degrés par rapport à une ligne horizontale.

Les résultats sont publiés ci-dessous[105]:

[105] H.Y.Liang, Z.L.Li, Z.X.Wang, W.Z.Wang, F.Rosei, D.L.Ma, H.X.Xu, *Small*, 2012, 8, 3400.

Dans la section V, nous nous sommes concentrés sur le renforcement de photoluminescence (PL) dans le système plasma / fluorophore comprenant des points quantiques (PQs) de chalcogénure de plomb et le film de nanoparticule (NP) d’Ag. Les films Ag-NP/PQ ont été fabriqués par une méthode de couche par couche. (Figure R6) Les films ont montré un renforcement important de la PL, dominé par le mécanisme de renforcement d’excitation lorsque les spectres des nanostructures d’Ag ne correspondent pas à la bande d’émission de PQs et la longueur d’onde d’excitation était loin du pic RPS dans le domaine du proche infrarouge (IR). En revanche, des

mécanismes de renforcement de l'excitation et des émissions pourraient contribuer au renforcement de PL lorsque les spectres d'absorption/émission de PQs correspondent à longueurs d'onde de résonance du film d'Ag. En outre, par l'optimisation du système Ag-NP/PQ, nous avons pu atteindre une CE aussi élevée que 2.8, grâce au fort couplage entre les PQs et nanostructures d'Ag. Par conséquent, ces films Ag-NP/PQ sont très prometteurs pour les dispositifs émergents de PQs pour les applications comme des diodes électroluminescentes avec haut rendement et les capteurs biologiques.

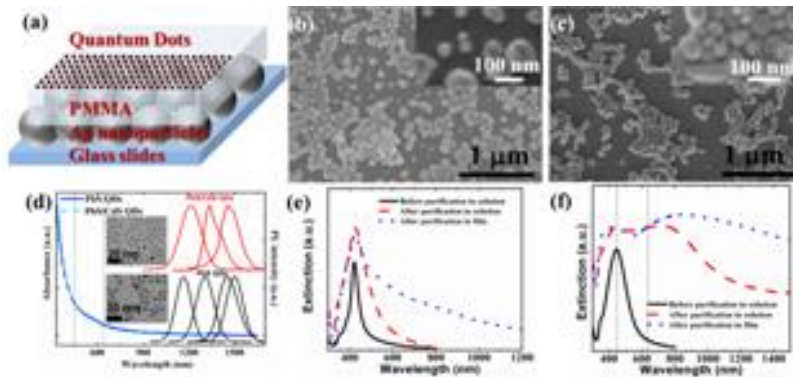


Figure R6. (a) Schéma d'un échantillon contenant PQs sur un film de NP d'Ag. Images MEB de (b) Films d'Ag#1 et (c) d'Ag#2. (d) Spectres d'absorption (à gauche) de PQs de PbS et PbS/CdS noyau/coquille avec pics de PL à 1500 nm et 1350 nm, respectivement, et les spectres de PL d'une série de PQs de PbS et PbS/CdS noyau/coquille. Encarts: images de MET de PbS PQs (en haut) et PQs de PbS/ CdS noyau/coquille(en bas). Les spectres d'extinction de (e) Ag#1 et (f) Ag#2 avant et après la purification dans la solution et après dépôt du film. Ils sont omis afin d'obtenir plus de clarté. Les lignes en pointillé à (d) et (f) dénotent l'excitation de 450 nm et 636 nm, respectivement.

Ce travail est décrit dans l'article ci-dessous:

Photoluminescence Enhancement of Near-infrared Emitting PbS and PbS/CdS Core/shell Quantum Dots Induced by Silver Nanoparticle Film, H.Y.Liang, H.G.Zhao, Z.P.Li, C.Harnagea, F.Rosei, D.L.Ma. En préparation.